Rate Dependent Strength Characterization of Carbon Fiber Composite Laminates

Jaspar Marek

A Thesis submitted in partial fulfillment
of the requirements for a

Master of Science in

Aeronautics and Astronautics

University of Washington

2017

Program Authorized to Offer Degree:
Aeronautics and Astronautics

University of Washington

Abstract

Rate Dependent Strength Characterization of
Carbon Fiber Composite Laminates

Jaspar Marek

Chair of the Supervisory Committee:
Department Chair Anthony Waas
Committee member: Professor Jinkyu Yang

The implementation of carbon fiber laminates in commercial vehicles is becoming increasingly common. Characterization of these materials for modeling is often completed at quasi-static loading rates regardless of the loading rates the final part will experience. This thesis will discuss the rate dependency of strength characteristics and Schapery parameters of a composite laminate under quasi-static, intermediate, and high rate loading conditions.

TABLE OF CONTENTS

Page

LIST OF FIGURES

ACKNOWLEDGMENTS

I would like to express sincere appreciation to Professor Anthony Waas for providing guidance throughout the research process, Professor Jinkyu Yang for reviewing my thesis and defense as well as the University of Washington for the use of their facilities. I would also like to thank Affiliate professor Mostaffa Rassaian, Salvatore Liguore, Brian Justusson, and Joseph Schaefer of The Boeing Company for their financial support and research guidance throughout the course of my studies.

Additionally I would like to thank the PhD students and post doctoral researchers, Solver Thorsson, Dr. Nhung Nguyen, Dr. Royan D'mello, and Ashith Joseph, that provided mentorship in my work throughout its duration.

Finally I would like to thank my family for supporting me in my academic exploits throughout all these years.

Chapter 1

INTRODUCTION

1.1 Objectives

The common practice for modeling of carbon fiber composite materials is to use the material properties gathered at quasi-static loading rates. These material characteristics are then applied to models for impacts and vibrations that occur at much higher rates of strain and expected to deliver accurate results. This method of modeling has become commonplace due to the lack of quality testing at elevated strain rates. Recently high rate testing data acquisition techniques have greatly improved allowing for new analysis to take place. Even with these improvements no consistent results have been shown regarding the effect of high strain rates on carbon fiber composite laminates.

This thesis will show the effect of applied strain rates on a material system across multiple rates of applied strain and multiple layups in both tension and compression. The strain to failure, failure load, and stiffness values gathered from each of these tests will then be compared across the applied rates and used as input parameters for a failure criteria in a predictive model. Validation testing will then be presented to verify the model. In this thesis I have selected one modeling failure criteria, Extended Schapery Theory (EST) developed by Professor Waas and Evan Paneda[4].

EST is a failure criteria based on the thermodynamic work potential principles of energy absorption and requires that the stress-strain curve shows pre-peak non-linearity. This non-linearity is indicative of micro-cracks in the specimen whose formation can be clearly seen in quasi-static testing. However due to technological restrictions the formation of micro-cracks at higher strain rate testing as not been captured. In this thesis I will demonstrate the high rate formation of micro-cracking and the transition to macro-cracks.

1.2 Topics Covered in the Thesis

The aforementioned topics will be addressed throughout this thesis in the following chapters:

Chapter 2: Design and Calibration of a Split Hopkinson Bar-
This chapter will introduce the basic theory behind both tensile and compressive Hopkinson bar testing. The design behind both the tensile and compressive bar will be discussed and illustrated. A tensile bar was designed and constructed for the purposes of this thesis, the calibration and post processing method used for the recorded data will be introduced.

Chapter 3: Determining Rate Dependance of Carbon Fiber Laminates-
Testing results of three laminate material systems ($[\pm 45]_s$,$[\pm 30]_s$,$[+15]$) in tension, and one material system in compression ([90]) will be shown across three applied strain rates: quasi-static(1e-5/s), intermediate(0.2/s), and high rates ($> 10/s$). The results, including failure loads and strains will be discussed, showing the effect on each material system of increasing the applied strain rate.

Chapter 4: Validation of Micro-Cracking at High Strain Rates through Strain Localization-

Using a new generation of high speed camera additional iterations of testing were preformed on the $[\pm 45]_s$ material system. The camera allowed for higher resolution images to be captured at higher frame rates than previous testing. These images provided a much more clear demonstration of strain localizations, illustrating the formation of micro-cracks in thick specimens where two piece failure was not observed. Testing also captured the formation of macro cracks in thin specimens rather than a single failure event.

Chapter 5: Determining Schapery Parameters-
This chapter will introduce Schapery theory as a thermodynamic work potential failure model. A step by step discussion of how the parameters are derived from testing data for each mode of failure is then provided using the tests completed in the pervious chapter.

Chapter 6: Application of Measured Material Characteristics to a Predictive Model-

This chapter will present a predictive model that is a result of the culmination of the previous four chapters. Using the measured at rate failure criteria from chapter 2, and the Schapery parameters calculated in chapter 5 an Open Hole Tension model was created for three different material systems. These models were then validated with testing of OHT coupons constructed of each of the material systems. The models input parameters were then re-evaluated for increased accuracy.

Chapter 7: Conclusion and Discussion-

Conclusions of test data and a discussion of testing recommendations, as well as potential future work will be discussed in this chapter.

1.3 Contributions

The study of composite materials at elevated strain rates has produced mixed results across researchers testing techniques. The commonly presented testing method for axial testing at elevated strain rates is the Split Hopkinson Bar, even with a consistent apparatus a large variety of methods are used to produce a loading pulse and mount a test specimen. This thesis presents four major contributions to the field of at rate composite laminate testing:

1) A consistent method to grip specimens and produce repeatable test results at high strain rates on the Split Hopkinson Tensile Bar.

2) Proof of micro-crack formation prior to macro-crack formation and propagation at high strain rates

3) A full characterization of a Carbon fiber composite laminate material system across three applied rates of strain.

4) An analysis of the effect of strain rate on Schapery Theory parameters.

Chapter 2

DESIGN AND CALIBRATION OF A SPLIT HOPKINSON BAR

2.1 Introduction

Traditional material testing is conducted at quasi-static loading rates ($10e-4$ strain/sec) using hydraulic or screw driven testing frames. While these frames provide both load and displacement data throughout the duration of a test, the strain rate at which tests executed is limited to a certain displacement rate. High rate uni-axial test are commonly preformed on materials using a Split Hopkinson Pressure Bar (SHPB) for compression tests, and a Split Hopkinson Tensile Bar (SHTB) for tensile testing. These testing devices are designed to operate under the assumptions of one dimensional wave theory, allowing the specimen to achieve a dynamic equilibrium at a constant strain rate. When these assumptions are met the dynamic stress-strain response of the tested material can be derived.

Each material that is tested at high rates is expected to have unique strength and failure properties, it is necessary to account for these properties in both the design of the Hopkinson bar that will be used to test them, as well as the dimensions of the specimens. This chapter will discuss the Hopkinson bar theory and provide an overview of how both a SHPB and SHTB were designed, built, and calibrated along with the design iterations that were implemented for improved testing performance.

2.2 Split Hopkinson Bar Theory

Split Hopkinson bars (tensile or compressive) are constructed of three main components: a striker, an incident bar, and a transmitted bar. The specimen that is to be tested is mounted between the two bars, then the striker provides a one dimensional wave at the free end of the incident bar. The wave then propagates through the bar, through the specimen and finally through the transmitted bar. Strain gages are placed on both the incident and transmitted bars to gather data throughout the duration of the test. The dimensions of the specimen are

chosen to provide the largest possible strain rate while maintaining a uniform deformation across the gage section and minimizing any potential width effects. The dimensions of the bars are chosen to maximize the recorded strain wave while fitting within the recommended dimensions of a 1:80 diameter to length ratio, and a 1:3 striker to bar length ratio. These recommended dimensions ensure that any reflected waves, caused by interfaces (i.e. bar to specimen) or step changes in diameter (i.e. the addition of grips), are recorded separately from the initial loading pulse of the test. Once the bar is constructed these uniform strain conditions are checked by verifying that the measured incident strain is equivalent to the reflected and transmitted strains.

$$\epsilon_I(t) = \epsilon_T(t) + \epsilon_R(t) \tag{2.1}$$

When the strain equilibrium presented above is verified the SHB can be calibrated for testing. Each test is analyzed using only the initial pulse created by the striker. Any successive pulses are generated through reflections or noise in the system such as specimen cracking or failure. The initial pulse travels through the incident bar, then the specimen, where it looses energy as the specimen fails. The transmitted pulse is then used in combination with the known material properties of the bars to determine the stress experienced in the specimen during loading(2.2).

$$\sigma_s(t) = E(\frac{A_0}{A}) + \epsilon_T(t) \tag{2.2}$$

$$\epsilon_s(t) = -(\frac{2C_0}{L}) \int_0^t \epsilon_R(t)dt \tag{2.3}$$

Where E is the Young's modulus of the steel bar, A_0 is the cross sectional area of the specimen, A is the cross sectional area of the bar, and C_0 is the speed of sound through the bar material.

The strain in the specimen can be derived through a relation with measured reflected strain in the incident bar (2.3). However it has been shown that while this method can be used for metals it is inaccurate for determining the strain in composite materials. Consequently the strain on the surface of the composite specimen was measured using Digital

Image Correlation providing a more accurate strain measurement while also providing a visual check that the specimen is uniformly loaded. The tests completed in this thesis used DIC analysis to measure the strain experienced by each tested specimen, and the measured transmitted strain to calculated the stress experienced by the specimen. The two data sets were then matched according to peak loads and duration to achieve a stress-strain relationship.

2.2.1 Split Hopkinson Pressure Bar

The SHPB used for testing in this thesis was constructed of three steel bars: a 182mm long, 12.7mm diameter incident bar, a 122mm long 12.7mm diameter transmitted bar, and a 30.5 mm long, 12.7mm diameter striker bar. The striking end of the striker bar and the struck end of the incident bar were slightly chamfered to minimize deformation throughout repeated testing. The striker was placed within a barrel machined to have a sliding fit around the bar. The striker rod is loaded into the back of the pressure barrel, compressed gas is released into the chamber, causing the rod toe be driven out at high speeds and impact the incident bar (2.1). The incident and transmitted bars are fixed to a testing table collaterally and allowed to move in the loading direction through unidirectional bearings. This allows the impact to transmit a compressive wave through the incident bar, specimen, and finally the transmitted bar.

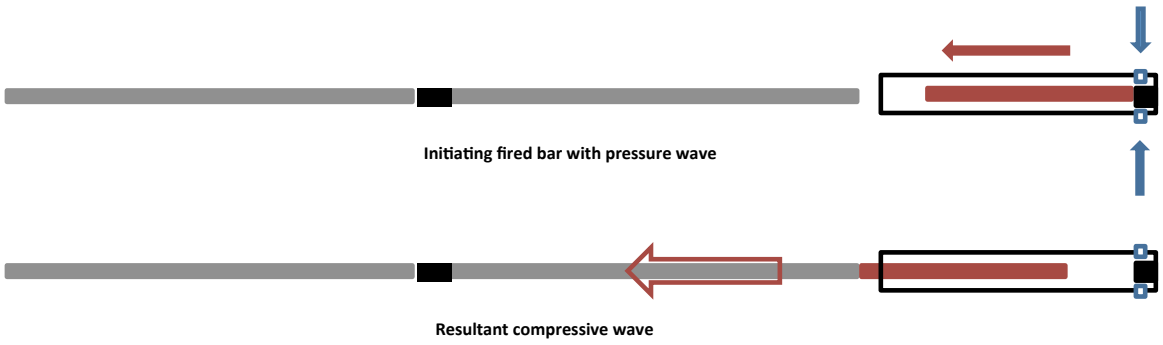

Figure 2.1: Demonstration of SHPB Mechanics

Common SHPB testing techniques of homogenous materials 'mounts' the specimen between the two bars using a thin layer of viscous material to minimize impedance. This method has been shown to induce brooming at the edges of composite laminates and results in inaccurate failure stress, and failure strain measurements. The specimens tested in this thesis were potted in grips (2.2)ensuring that the failure occurred within the gage section of the specimen and providing a similar boundary condition (bounded) to the clamped edges of the quasi-static testing in a Wyoming Combined Loading Compression fixture.

Figure 2.2: Grips used for SHPB testing

Strain gauges were attached to both the transmitted bar and the incident bar at equivalent distances of 40 mm form the specimen interfaces. These gauges were used to measure the strain time history of the compressive wave traveling through the bar. The stress time history of the specimen was then computed using the stress relationship presented above. A Photron Fastcam SA-X high speed camera in combination with a 105mm Sigma lens was used to capture images of the test for DIC analysis of strain and displacement data at 200,000 frames per second.

Initial testing was completed on aluminum specimens to achieve repeatable results as well as a base line for bar speed v. firing pressure. Using the speed v. pressure relationship an estimate could be made to achieve the desired loading rate of the specimen, and the resultant strain rate. Dummy specimens were then tested to determine the effect of different potting methods.

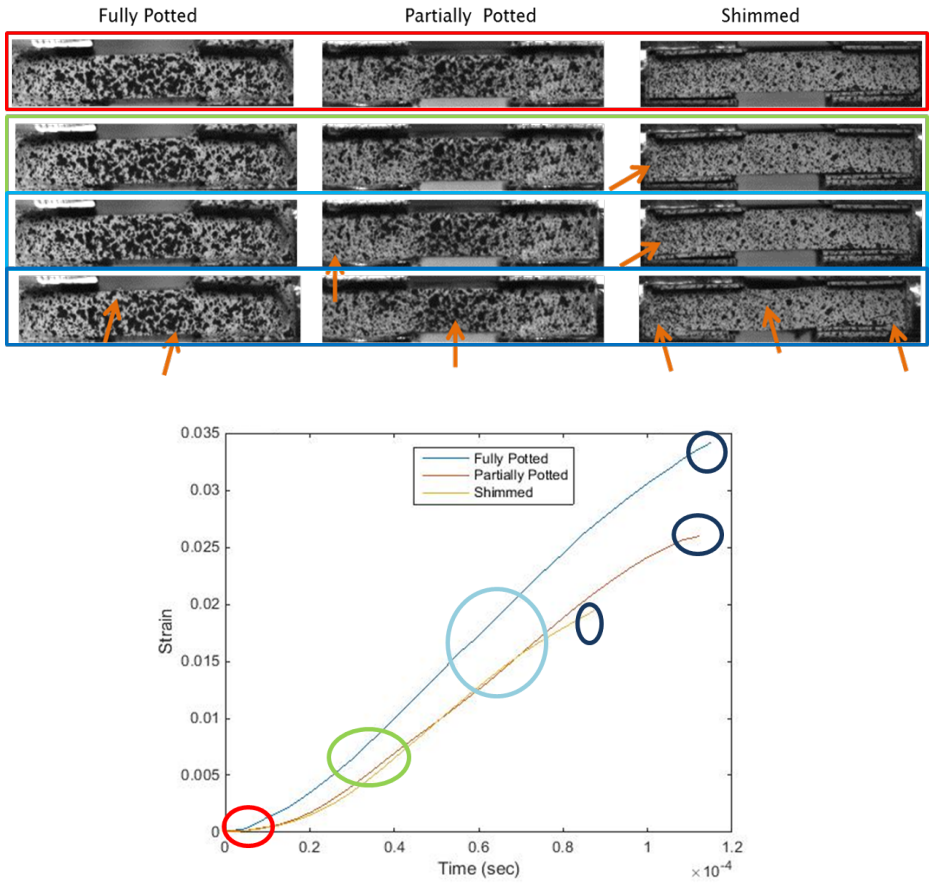

Figure 2.3: Analysis of Potting methods used for SHPB testing

Three cases were tested to verify that potting the specimen produced the correct material response with reliable results and no localization of the strains induced by the potting (2.3). In the he first case the specimens were placed in the grips and shimmed, the second case used high shear strength HYSOL E20HP epoxy to lightly bond the shims and the specimen together, the third case used the shimming to place the specimen in the grips and the epoxy to fully pot the ends of the specimen. in both cases one and two the specimen shifted within the grips during the test resulting in an inconsistently applied load and localized strains outside of the gage section. These localizations produced early failure and incorrect measurements. The fully potted specimens showed uniform strain distributions throughout the test with a final failure limited to the gage section. The fully potted case was then

adopted for the testing to follow.

2.2.2 Split Hopkinson Tensile Bar

The SHTB is comprised of the same main components as the SHPB with the addition of a momentum trap. The SHTB is then constructed with the pressure barrel facing the opposite direction as the SHPB as to create a tensile pulse within the bar. The incident bar is attached to the testing platform with linear copper bearings allowing it to slide freely in the loading direction. The bar passes through the striker and the pressure barrel which are concentric. The incident bar then terminates with a flange the same diameter as the outer diameter as the striker tube. Pressurized air is passed into the barrel forcing the striker tube out and into contact with the flange which is in contact with a pulse shaper and a momentum trap. The pulse shaper is used to minimized reflective noise of the impact, while the momentum trap absorbs the linear motion of the bar, allowing the specimen to be loaded in local tension with no global translation. The resultant pulse travels back down the incident bar in the form of a tensile wave, passing through and loading the specimen before passing through the transmitted bar. One strain gauge is placed on each bar equidistant from the specimen to record the strain time history of the test, while a single Photron Fastcam SA-X high speed camera focused on the surface of the specimen and recorded images at 200,000 frames per second for DIC analysis.

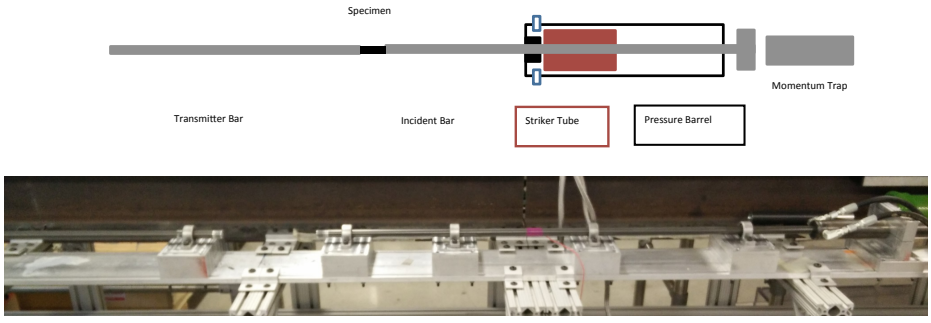

Figure 2.4: Illistration of SHTB setup

The high rate tensile testing completed in this thesis was all completed on a SHTB

designed, built and calibrated specifically for the tests. It is important to note that for each change in specimen dimensions, or material characteristics it is necessary to validate the design of the SHTB. Each material tested has unique properties that influence the displacement to failure and the load at failure. As the displacement to failure increases a longer striker tube is needed, as the load to failure increases a more massive striker tube is necessary. Along the same lines, if a smaller failure load is expected the bars material must be sensitive enough to transmit a measurable signal both through the specimen and strains gauges to gather usable data. Additionally under repeat loading the incident bar will fatigue, effecting its ability to transmit a repeatable pulse, the number of uses of a bar must be tracked to ensure the bar is replaced when necessary.

2.3 Design of a SHTB

When performing a quasi-static or intermediate strain rate test the specimens are tested in a hydraulic or screw driven loading frame capable of a large displacement. Throughout this displacement the load is recorded using a piezoelectric load cell while the strain is captured using a speckle pattern to be processed using DIC at a later point. At low rates of strain the material is allowed to plastically deform or 'shift' under low loads, however as the applied rate increases the material has less time to 'shift' and adjust to the applied load.

Using the results of the quasi-static and intermediate rate testing as reference points for the expected displacement to failure of the laminates a SHTB was designed. The striker tube length determines the length of the tensile pulse that will be transmitted through the bar. The data gathered for the test can only be gathered within this initial pulse so it is necessary that a long enough and massive enough striker tube is chosen to fail the specimen. The initial tests were conducted on the $[\pm 30]_s$ and $[+15]$ specimens using a 12" steel striker tube with a 1.25" OD and a 0.75"ID. The striker tube was fired from a 1.75" OD , 1.25" ID Drawn Over Mandrel(DOM) pressure barrel 36" in length. It is necessary to use a DOM barrel to ensure the interior is smooth, allowing a smooth surface for the striker tube to slide along. The incident bar was constructed from a $\frac{3}{4}$" diameter, 84" long steel bar with a 1.25" diameter flange screwed onto the end. Previous SHTB testing has established that an incident bar that is three times longer than the length of the striker tube is sufficient to

establish clear separation between the incident pulse and any trailing tensile or compressive wave formed as a result of reflections. All surfaces of the system were lubricated with low viscosity, tight tolerance machine oil, minimizing friction in the system.

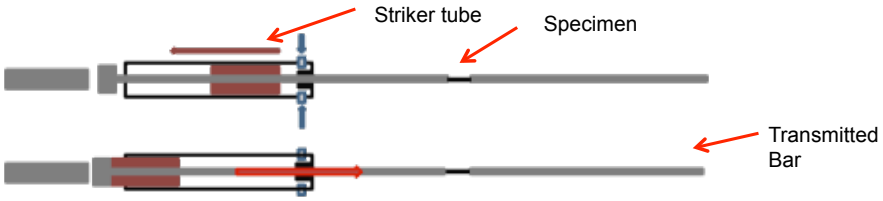

Figure 2.5: Illustration of SHTB Mechanics

Testing of the [±45] laminate required a significantly larger displacement to failure, an as a result required a much longer pulse and striker tube. The striker tube was change to a 24" long steel tube with 1.25"OD and 0.75"ID. In order to ensure the striker tube velocity would remain sufficiently high enough to fail a specimen the pressure barrel was also extended to 72" with the same inner and outer diameters as the prior barrel. The incident bar was still sufficiently long enough to observe a separation of pulses so remained the same.

Both bar setups utilized a transmitted bar of the same dimensions ($\frac{3}{4}$" diameter x72" long) and mounted the specimens using the same grips. The method used for gripping specimens in a SHTB is incredibly important to the quality of data that can be gathered from the testing. Every interface or change in cross-sectional area in the path of the transmitted pulse absorbs and reflects part of the pulse. In addition any change in material (i.e. bonding agents or epoxys) will absorb energy of the pulse, this energy absorption causes the 1D wave theory analysis will not hold. Previous high rate testing literature has showed three consistent gripping methods: wedge grips, potting, and pinning. The wedge grips introduce multiple interfaces between the bar and the specimen causing a large potential for signal loss, as well as requiring significant pre-tensioning of the grips to ensure transmission will take place. Potting the specimens introduces a new softer material that also absorbs a large amount of energy before it is transmitted through the specimen. The pinning method can

introduce stress concentrations within the grips and premature failures.

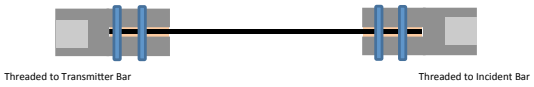

Figure 2.6: Illustration of SHTB Grips

The grips used for testing were constructed from 1.25" diameter cylinders with a machined $\frac{3}{4} - 16$ female thread into one end. The grip will then thread onto the male threaded free ends of the incident and transmitted bars. The grips were machined in sets of 5, each set was machined with a slit the thickness of each laminate on the opposite end of the threading. The slit end was then drilled through with two holes for 0.25" pins to be placed through both the grip and the specimen. The specimens were potted into the grips, then drilled, then pinned. The pins ensure that the load is cleanly transmitted though the specimen while E20HP high shear strength epoxy was used to pot the specimen and ensure that no stress localizations occurred within the grip.

2.3.1 Calibrating a SHTB

The construction of a new testing apparatus requires calibration of the test frame in order to verify the testing method and ensure that it was designed properly for the intended function. The initiation of the pulse must be consistent to provide repeatable results, the magnitude and duration of the pulse is determined by both the length of the striker tube and the velocity at which it impacts the flange. Initial testing of the firing mechanism was conducted to establish a repeatable trend for the correlation between firing pressure and the striker bar speed. A high speed camera was used to record the exit of the striker tube from the barrel and the impact of the flange, the distance between these two points was kept constant throughout testing, this provided a repeatable condition for striker bar velocity measurement during calibration.

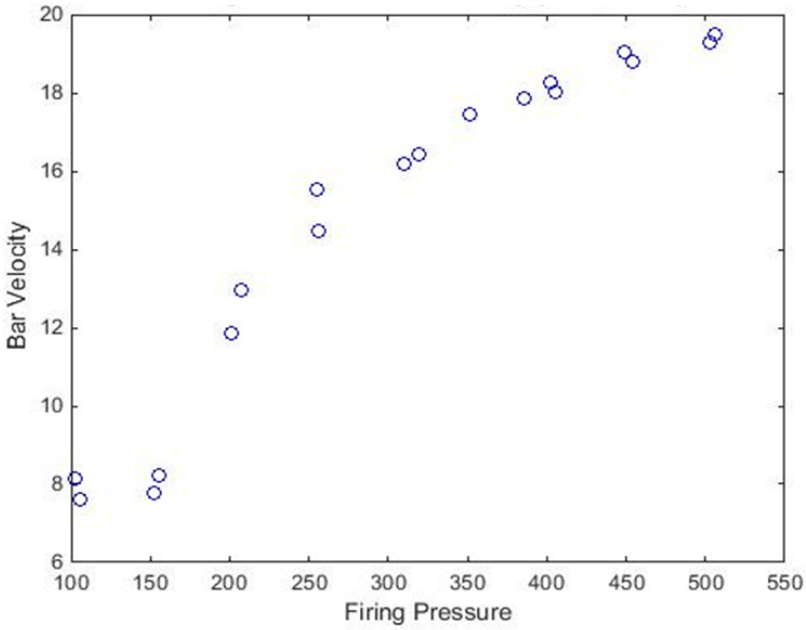

Figure 2.7: Striker Bar Velocity v. Firing Pressure

the length of the striker tube creates a plateau region of equivalent length in the tensile wave, while also allowing separation between the primary wave and any subsequent waves and reflections. Using elastic wave theory a X-T diagram was constructed to model the expected behavior of the SHTB when a wave was being transmitted. This diagram ensured that a clear signal could be transmitted through the specimen and transmitted bar to be recorded before any reflections altered the data.

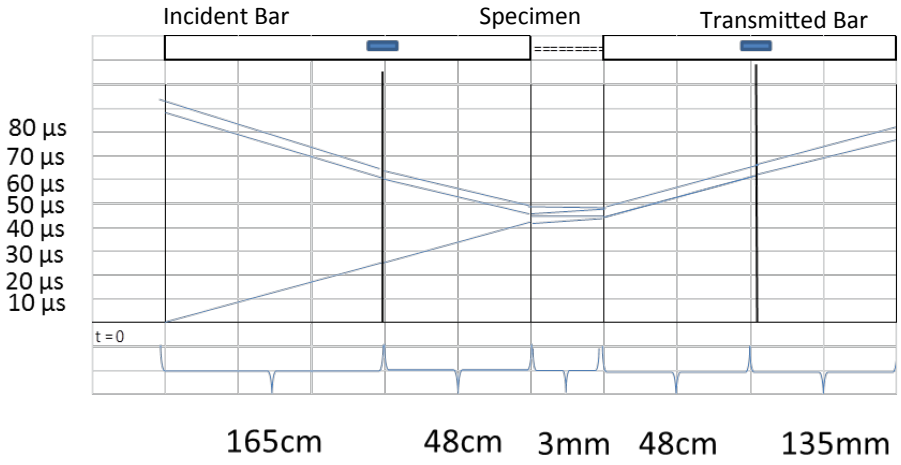

Figure 2.8: Plot of Waves transmitted though the testing apparatus as a function of distance X and time T

To ensure these calculated values were being achieved on the test frame a benchmarking process was first followed. Previous work completed by [1] established consistent results with OFE C10100 Copper using a SHTB, and recorded the strain using DIC software. Using the same dog-bone dimensions as Gilat presented testing began with potted specimens and no pins. These results showed a weak transmitted signal due to the epoxy absorbing energy form the transmitted wave. The specimen gripping area was then increased to allow pin holes to be drilled, the tests were pinned are repeated, producing a much larger transmitted pulse. The transmitted wave shown in the second round of tests did not show a plateau region. To ensure that the pulse reached a plateau region the momentum was made more rigid by fixing a large mass behind the trap. this change produced a nice trapezoidal shaped pulse and allowing the reproduction of the expected stress-strain curve for Copper.

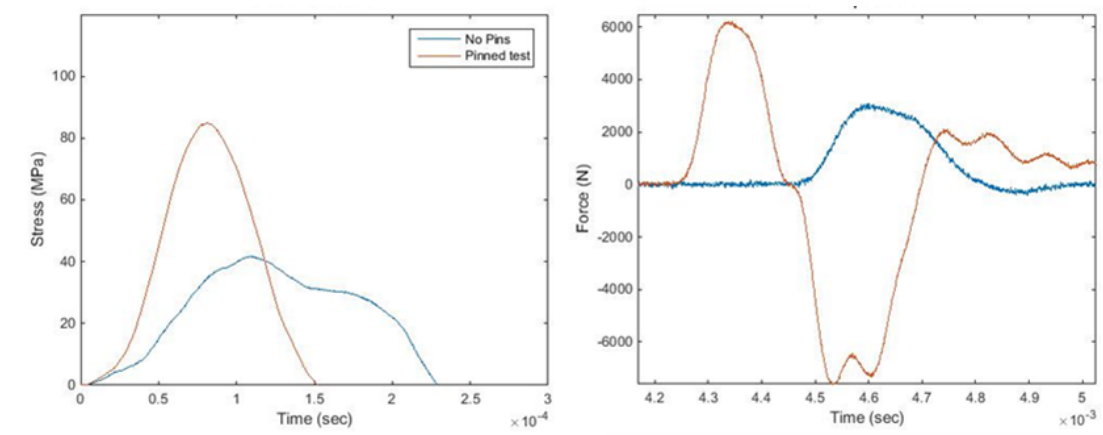

Figure 2.9: Pinned v. Unpinned load v. time pulses (left), Incident and transmitted pulse (red and blue respectively) of pinned specimens with momentum trap.

2.4 Post Processing of SHTB and SHPB data

Using a SHPB and a SHTB for high strain rate testing is a widely used and accepted practice for metals and other homogeneous materials. These materials allow for a direct application of one dimensional wave theory to a test with minimal error. Testing of composite structures at high rates has been completed using Hopkinson bars as well, however because composite structures are composed of multiple materials the one dimensional wave theory can only be applied when no damage is present in the structure and it behaves as if it were homogenous. As soon as macro-damage forms the signal transmitted through the specimen is altered in multiple ways causing the recorded test data to become an inaccurate representation of failure events in the specimen. Most published work on Hopkinson bar testing of composites fails to address how a stress-strain curve was constructed from the gathered data, only citing the one dimensional wave theory. This section will discuss the methods I used to create a stress-strain curve, and the reasoning behind each step in an effort to address this often glossed over topic.

2.4.1 Stress Calculation

At the beginning of the test the carbon fiber laminate is treated as a homogenous material that will allow a one dimensional wave to uniformly travel through it, and into a transmitted bar where the signal is recorded. As the magnitude of the wave increases the load on the specimen also increases (**??**). As the load increases micro-cracks form in the specimen, this progressively decreases the rate of load increase until a macro-crack is visible. This point is taken as the peak load that is recorded on the transmitted wave, after this point the plateau region of the curve cannot be used as the specimen is too damaged to transmit a signal that represents anything other than noise. The transmitted wave is recorded at at known sampling frequency, providing a stress-time relationship that can be matched to the strain data.

2.4.2 Strain Calculation

The material testing presented in this thesis was completed using Digital Image Correlation (DIC) techniques for strain measurement. A fine speckle pattern was applied to the surface of each samples gage section using matte white paint as a base, and matte black spray paint for the speckles. Once the specimen was mounted between the incident and transmitted bars a high speed camera was focused on the gage section allowing the duration of the test to be captured at 200,000+ frames per second. Using the Aramis software package to process the images a line strain was measured across the gage section of the material. The line strain technique uses the initial image as a reference (i.e. zero strain) then tracks the change in length of the line throughout all the recorded images, providing a strain-time relationship. This data is then truncated to the point at which the first macro-crack is visible on the test images.

2.4.3 Combining Stress and Strain Data Sets

The final step in the construction of a stress-strain relationship is dependent on the time history alone. The point at which a macro-crack is first observed is taken as the ending time stamp of the test, while the point at which the strain rises above zero strain is taken

as the initial time stamp. The difference between these two points on the strain time curve is the duration of the test. Starting from the peak of the stress-time curve the test duration is then used to determine the initial loading point of the test. With the two sets of data appropriately matched with respect to time a stress-strain curve is constructed (2.10). Because the two data sets must match with respect to time it is pivotal to ensure a quick and uniform rise time is created with the striker bar, and the specimen gage section will deform uniformly when strained. Any deviation of the rise of the transmitted wave, or irregularity in the deformation of the test specimen will alter the shape of the respective curve, resulting in a stress-strain relationship that presents misleading information.

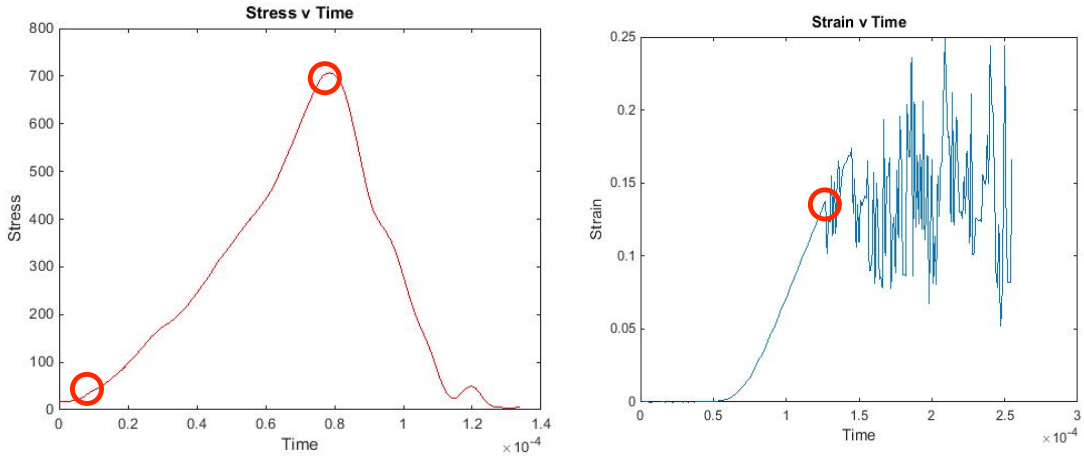

Figure 2.10: Stress v Time (Left), Strain v. Time (Right) with Start and end points highlighted

Chapter 3

DETERMINING RATE DEPENDANCE OF CARBON FIBER LAMINATES

3.1 Introduction

Previous testing of carbon fiber composites at high rates in both tension and compression have shown a variety of results. The common trend across all previous studies is that the material shows an increase in stiffness as the applied strain rate increases. This is commonly shown with an increase in the failure stress i and the a decrease in the strain to failure. Quasi-static (1e-5 strain/ sec) and intermediate (0.2 strain/sec) strain rates were tested on hydraulic load frames with high precision and repeatability. High rate testing (>10 strain/sec) is often run on Split Hopkinson Bars as discussed in Chapter 2. The Hopkinson bar apparatus requires constant maintenance and calibration. The incident and transmitted bars need to be retired after multiple tests to ensure that the signal is not being passed through fatigued material, and each test needs to be analyzed to ensure that a uniform strain is passing through the gage section of the specimen. The following chapter will discuss the results of high rate testing of three laminate layups in tension, $[\pm 45]_s$, $[\pm 30]_s$, $[+15]$, and one laminate in compression $[0/90]_s$. Multiple high rate tests were preformed to establish an average representative curve, this curve was then used to compare the high rate tests to the testing results of quasi-static and intermediate loading rates completed previously on a hydraulic load frame

3.2 $[\pm 45]_s$ *Laminates*

Tension testing of $[\pm 45]_s$ laminates was conducted at quasi-static, intermediate, and high rates. The testing was conducted to determine the Schapery micro-damage parameter g_s , the shear stiffness G_{12} and the shear failure strain 'Z' at each applied rate. Five tests were conducted at each rate, using the resultant stress v. strain curves an average representative

polynomial curve was constructed for each rate. The curves of the three rates were then compared to determine the effect of strain rate on the laminate. The high rate tests were conducted on the SHTB using a dog bone specimen based on the specimen dimensions used by Gilat et. al. [1]. Small increases in the width of the gage section were necessary to allow for multiple full fiber lengths to fall within the gage section, figure 3.1.

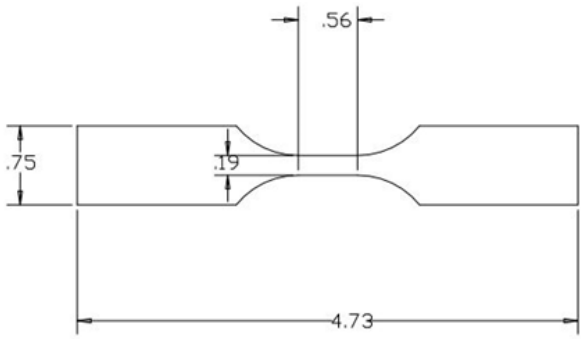

Figure 3.1: Dog bone specimen dimensions for high rate tensile testing of ±45 specimens

The five high rate specimens tested at an average strain rate of 401 /sec ±59.8. The tests will be compared on a normalized plot where the test with the largest peak shear strain value was set as a baseline shear strain and shear stress values. The average shear strain at lamina failure was 93.8% ±5.4 of the maximum recorded value while the average shear stress was 103.2 %±4.3 of the baseline value (3.2). All of the tests showed very close agreement and allowed for an accurate comparison of the high strain rate to lower strain rates. Testing of the $[\pm 45]_s$ material at high rates on the SHTB produced consistent lamina failure in the specimens, however no two piece failure was observed within the duration of each test. The quasi static and intermediate rate tests were conducted until full failure and demonstrated a much larger displacement at that point. For comparison purposes these data were truncated to the point the first macro-crack was visible, in the same manor as the high rate tests. The visible lamina failure is evidence of macro-cracks, signifying the end of the application of Schapery theory, allowing the calculation of the micro-damage parameter

'g_s' and the shear stiffness to be calculated.

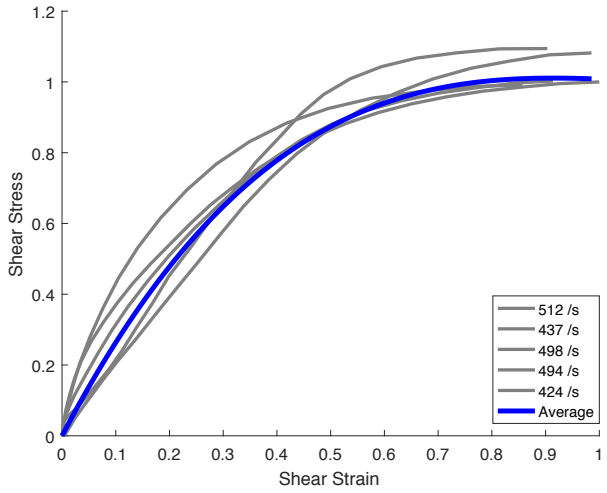

Figure 3.2: Comparison of high rate ±45 shear stress v. shear strain curves

Strain Rate (/s)	Shear Strain (γ)	Shear Stress (τ)
512	90	109
437	98.5	108
498	91.3	100
494	85.6	99
424	100	100
Average	93.8	103.2
Standard Deviation	5.4	4.3

Table 3.1: Comparison of high rate shear strain and shear stress failure points across $[\pm 45]_s$ laminate tests

Testing at quasi-static and intermediate strain rates was conducted on a hydraulic load frame with much larger displacement capabilities. These tests show visible macro cracks

where a plateau region forms on the curve, similar to the high rate testing (3.2). For comparison purposes the data was truncated at this point, while the tests were conducted to a full two piece failure at a much larger strain.

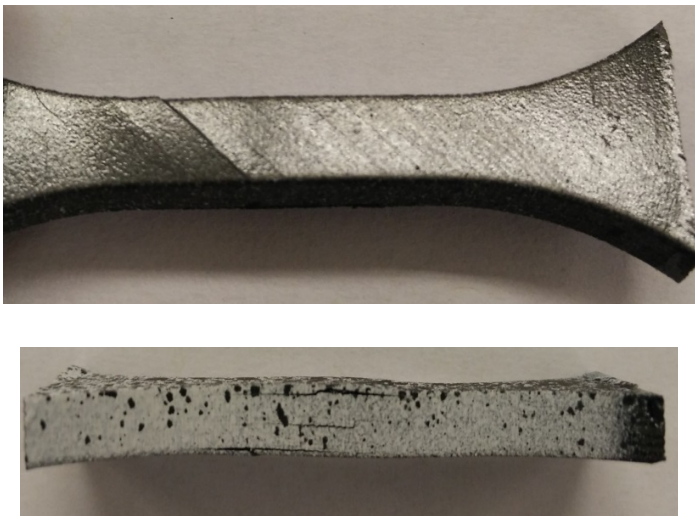

Figure 3.3: Macro cracks in High rate test specimen

Image of quasi-static test specimen macro cracking will be added soon.

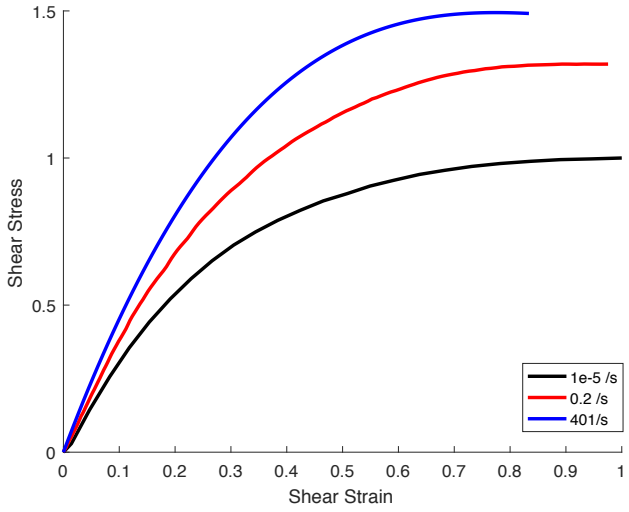

Figure 3.4: Comparison of ±45 shear stress v. shear strain curves across applied strain rates

Strain Rate	Axial Failure Stress	Axial Failure Strain	Shear Failure Stress	Shear Failure Strain
1e-5 /s	100	100	100	100
0.2 /s	132.2	93.7	131.9	97.55
401 /s	147	78	149	82.5

Table 3.2: Comparison of failure strains and failure stresses across [±45] rate tests

The results of the quasi-static testing were taken as a baseline to compare against for both the failure stress and failure strain. Normalizing all the data off the baseline provides a clear representations of the behavior of the material across the three applied strain rates (table :3.2). Intermediate rate tests failed at an average axial strain 32.3% higher than the quasi-static tests and a strain 6.3% lower than the quasi-static rate. This stiffening trend was continued with the high rate testing, which demonstrated a 47% higher failure stress and a 22% lower failure strain. As mentioned previously the stiffening trend has been observed in some previous research, while other publications have determined no rate dependance of material stiffness. Using the results of [±45] laminate tests this material system demonstrated stiffing as a function of applied strain rate, this conclusion will be verified in the following sections with various layups.

3.3 *[*±30]$_s$ ***Laminates***

Tension testing of $[\pm 30]_{4s}$ specimens was completed to determine the Schapery micro damage parameters in compression (e_{sc}) The tensile test applies a linear displacement to the specimen, this displacement produces a transverse compressive stress in the principal material frame. Testing was completed in order of increasing applied strain rate, initial tests at each rate were compared to the trend of slower applied strain rates to ensure that a stiffening trend was observed, as was expected after completing the [±45] testing. The initial high-rate testing was completed using the same specimen dimensions as the [±45] testing. The results of these specimen dimensions showed a softening trend throughout the duration of the test as well as a much softer trend over all than both the intermediate and quasi-static applied strain rates. After further analysis it was determined that the specimens were

experiencing early failure do to a narrow gage section. The gage section was increased to 15mm (0.59") wide and 37.34mm (1.47") long eliminating the width effect.

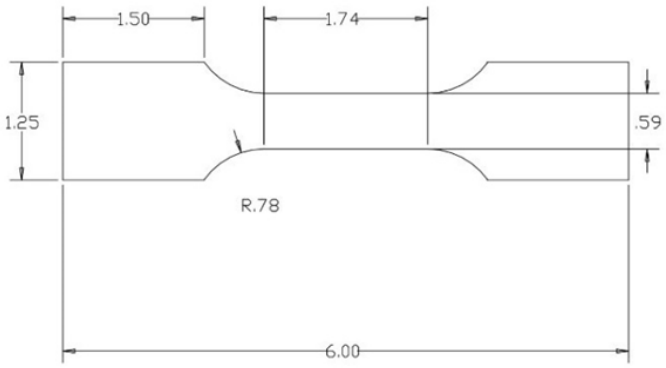

Figure 3.5: ±30 Dog Bond specimen dimensions for high rate tensile testing

Four tests were conducted at high rate using the SHTB these tests averaged 89.7 strain per second and showed very good repeatability. The four tests reached an average strain within 12% of the maximum strain and a average stress within ±3.65% of the maximum stress. Due to the large dimensions of the specimens in relation to the magnitude of the pulse created by the SHTB failure was not achieved within the duration of the test.

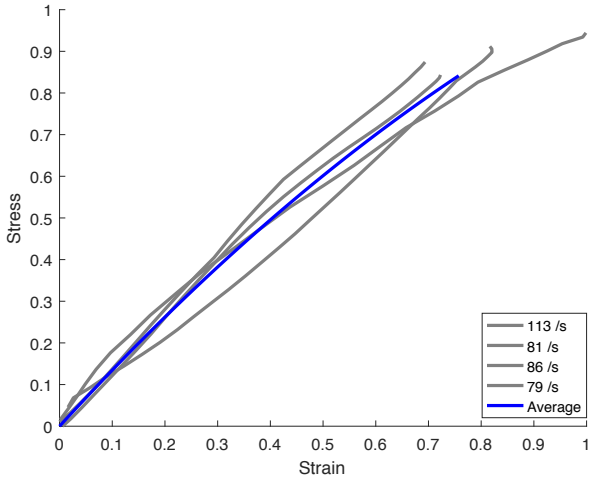

Figure 3.6: Comparison of ±30 Axial Stress v. Axial Strain Curves across applied strain rates

Strain Rate (/s)	Axial Strain (ϵ)	Axial Stress (σ)
113	100	100
81	82	96
86	72	90
79	69	93.4
Average	80.8	94.8
Standard Deviation	±12	±3.65

Table 3.3: Comparison of Axial strain and Axial stress failure points across $[\pm 30]_s$ laminate tests

Five tests were conducted on the [±30] material system at quasi-static and intermediate strain rates on a hydraulic load frame. As the applied strain rate was increased the material demonstrated a more linear, stiffer response. The increased linearity is representative of less micro-damage occurring as the rate increases (3.3). The stiffening trend with increased

linearity continues to be shown in the high rate tests. Because full failure was not reached in the duration of the test the high rate results cannot be directly compared to the intermediate and quasi-static values, however for visualization purposes a plot of the extrapolated high rate curve has been shown (3.3). The extrapolated plot shows that at high rates almost no micro-damage is expected to take place, a linear curve, and thus the application of Schapery theory is not possible.

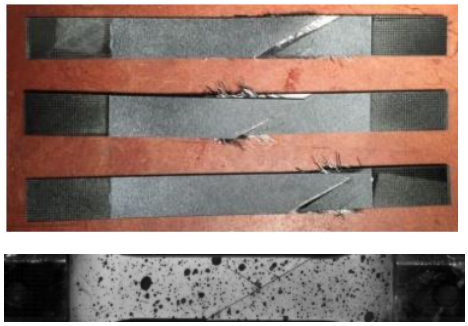

Figure 3.7: Comparison of failure modes of ±30 specimens, Top:Quasi-static and Intermediate rate, Bottom: High rate (failure occurred during compressive pulse)

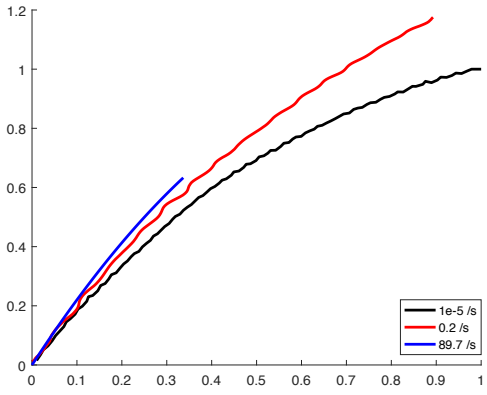

Figure 3.8: Comparison of Test Results across strain rates

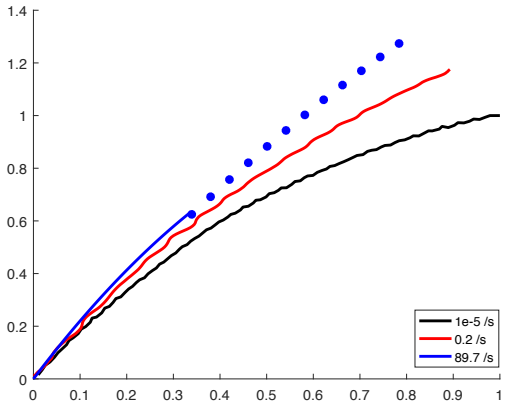

Figure 3.9: Extrapolated high rate curve compared to intermediate and quasi-static rates

3.4 +15 Laminates

Tension testing of $[+15^o]$ specimens was completed to determine the Schapery transverse micro-damage parameters (e_{st}) in tension, thus describing the evolution of the transverse stiffness $E_2 2$. Quasi-static and intermediate rate testing was performed on a hydraulic load frame using rectangular specimens (1" x 10") with a 6" gage section. High rate testing was completed on the SHTB using dog bone specimens of the same gage thickness as the $[\pm 30]_s$ testing (3.5), In order to allow the fibers to fall within the gage section the length of the dog-bone was increased to a gage length of 2.3". This increase in over all specimen dimensions allowed for a larger gripping area, and a much stronger transmitted signal, producing much more repeatable testing results.

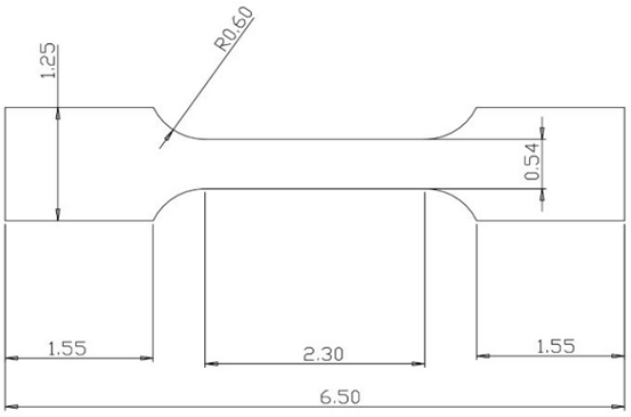

Figure 3.10: [+15] Dog bone specimen dimensions

An average representative curve was constructed for the [+15] laminate in the same fashion as the previous laminates. All eight test were plotted as a data cloud, the points were then fitted with a polynomial curve fit. The average curve shows that there was a 16.2% deviation in axial failure strains, and a 37.5% deviation in the axial failure stresses.

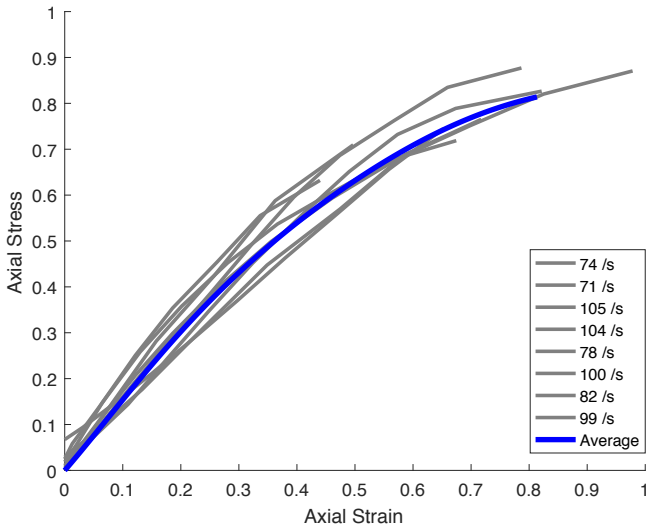

Figure 3.11: Comparison of High Rate +15 Axial Stress v. Axial Strain Curves

Strain Rate (/s)	Axial Strain (ϵ)	Axial Stress (σ)
74	84.4	95.6
71	80.8	98
105	46.1	76.2
104	74.1	89.5
78	67.4	87.5
100	52	83.9
82	69.6	85.1
99	100	100
Average	71.8	89.4
Standard Deviation	$\pm$16.2	$\pm$37.5

Table 3.4: Comparison of High rate Axial strain and Axial stress failure points across [+15] laminate tests

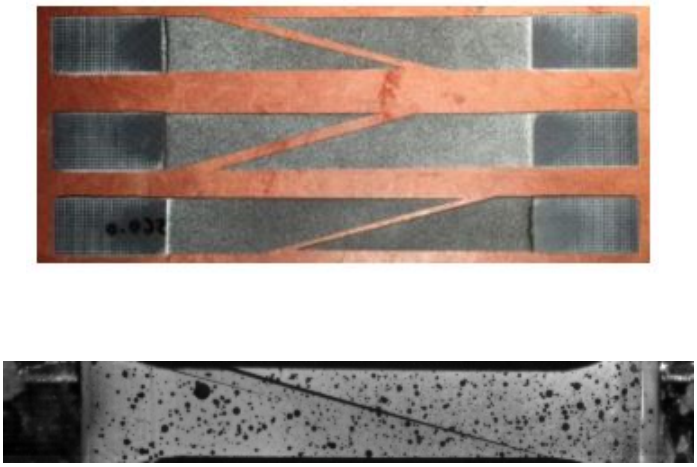

Figure 3.12: Comparison of failure modes of [+15] specimens, Top: Quasi-static and Intermediate rates, Bottom: High Rate

The $[+15^o]$ specimens demonstrated a stiffening trend, just as was shown by each of the previous layups. The quasi-static average curve was taken as a baseline for both failure stress and failure strain. The intermediate and high-rate average curves were then normalized against that baseline for comparison purposes. The intermediate strain rate showed a 0.3% lower failure stress and a 19.1% lower failure strain resulting in a more stiff material response than the quasi-static data. The high rate tests continued the stiffening trend with a failure strain 53.8% lower than the quasi-static tests, and a 20% lower failure stress. The high rate testing shows an initial linear stiffness, similar to the quasi and intermediate testing results, however it shows significantly more stiffness degradation near the end of the tests. The failure modes observed across all three rates were consistent (3.4) indicating that the observed change in stiffness was due to the applied rate and not other factors.

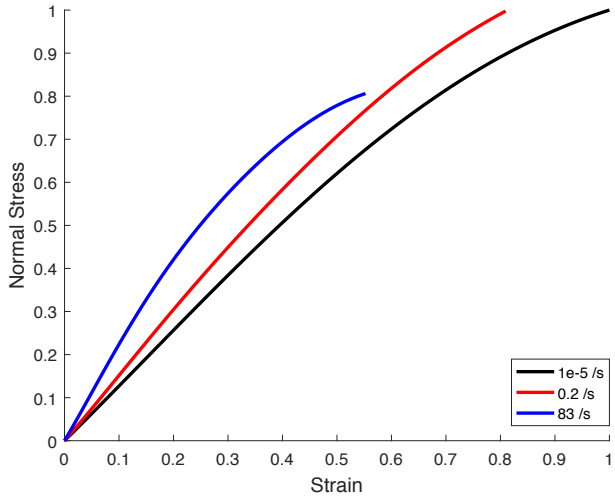

Figure 3.13: Comparison of +15 Axial Stress v. Axial Strain Curves across applied strain rates

Strain Rate	Failure Stress	Failure Strain
1e-5 /s	100	100
0.2 /s	99.7	80.9
104 /s	80.6	55.2

Table 3.5: Comparison of Axial strain and Axial stress failure points across [+15] rate tests

3.5 Transverse Compression

Testing on $[90_{32}]$ specimens was conducted to determine transverse failure strain in compression (Y_{22}^{c}). Quasi-static and Intermediate tests were conducted on a hydraulic load frame using a Zwick hydraulic composite compression fixture. The specimens were rectangular strips 5.5" long and 0.75" wide and a gage section 0.5" long. The high rate testing was conducted on a Split Hopkinson Pressure Bar with rectangular specimens 1.5" long by 0.75" wide. The high rate specimens were then potted on each end to prevent brooming, leaving a gage section of 0.5", the same dimensions as the gage section that as used for quasi-static

and intermediate rate testing Four tests were conducted at an average applied strain rate of 315 strain/sec, across the four tests a 10% deviation was observed in the failure stress and a 13% deviation was observed in the failure strains (table: **??**). All four curves show very similar stiffnesses throughout the duration of each test. The small variation in failure loads and strains can be attributed to slight differences in the potting of the specimens.

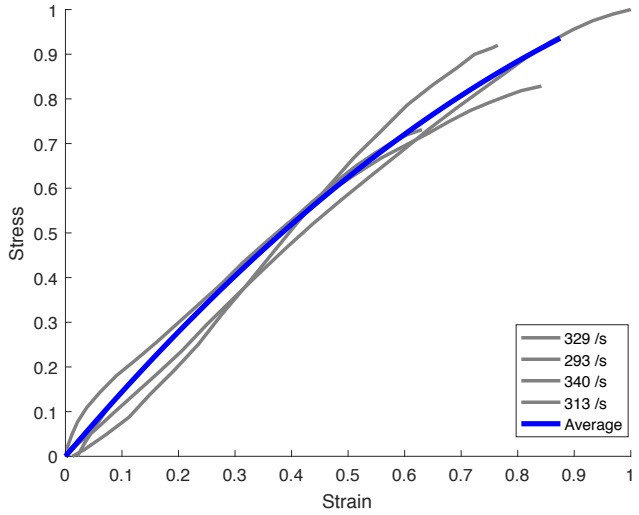

Figure 3.14: Comparison of High rate 90 Axial Stress v. Axial Strain Curves

Strain Rate (/s)	Axial Strain (ϵ)	Axial Stress (σ)
329	76.4	92
293	84.2	82.8
340	63	73
313	100	100
Average	80.4	86.9
Standard Deviation	$\pm$13.38	$\pm$10.09

Table 3.6: Comparison of High rate Axial strain and Axial stress failure points across $[90^0]$ laminate tests

The compression testing at high rates continued to show a stiffening trend as was observed in the tension testing. Across all applied strain rates the failure mode remained consistent, demonstrating the charictaristic chevron cracking shape of the $[90^0]$ laminate. The quasi-static and intermediate rate testing results showed a very similar stiffness up until half of the failure strain was achieved. At which point the quasi-static tests show significantly more softening due to micro-cracks, while the intermediate rate tests remain almost linear. The high rate testing also produced a very linear curve with a much stiffer trend than both the slower strain rates.

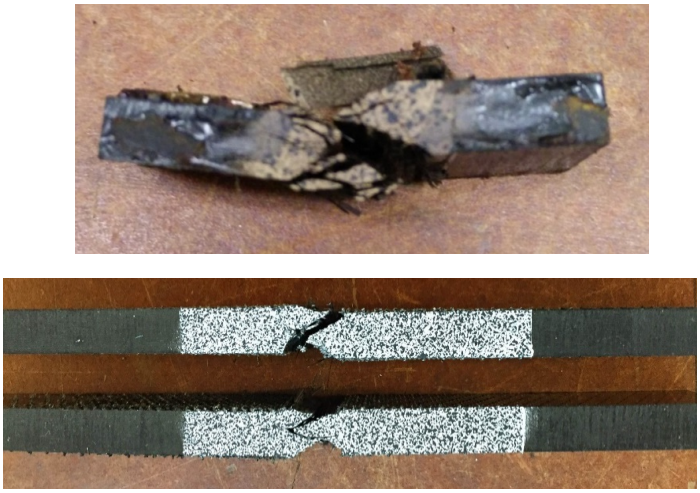

Figure 3.15: Comparison of failure modes across all rates, Top: high rage, Bottom: Quasi-static and Intermediate rates

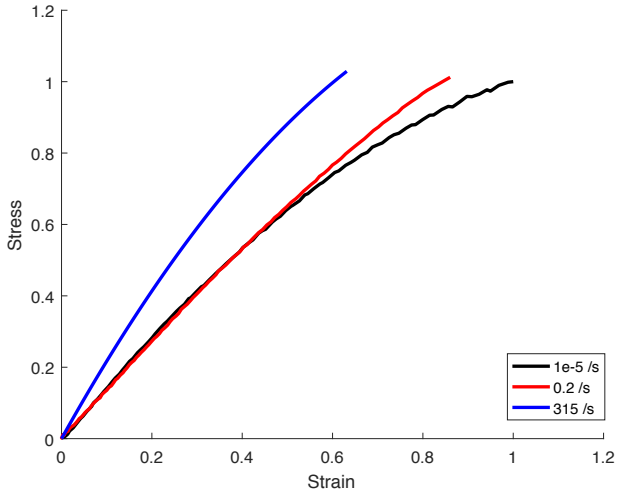

Figure 3.16: Comparison of 0/90 Axial Stress v. Axial Strain Curves Across Applied Rates

Chapter 4

VALIDATION OF MICRO-CRACKING AT HIGH STRAIN RATES THROUGH STRAIN LOCALIZATION

4.1 Introduction

Until recently recording DIC images at high rates of strain was limited by the low resolution images that cameras could capture. The low resolution of the images could be used to establish that a strain field was uniform throughout the initiation of loading, however the limited resolution was not able to capture strain localization due to micro-cracking. A new generation of Shimadzu high speed camera (HPVX2), supplied by Hadland imaging, only records 128 image for each firing, by limiting the number of images recorded the camera is able to record at a much higher resolution and maintain the resolution across all its available frame rates. With the increased resolution of the images a detailed strain field could be constructed using DIC that showed strain localization due to micro cracks as well as the initiation of macro-cracks and the propagation of those cracks until full failure of the specimen. Testing in this chapter was conducted on two sets of specimens, a pair of tests was completed on 16 ply thick [$\pm$45] specimens to show the initiation of micro-cracks and the transition to macro-cracks. Multiple tests were then preformed on a thinner 8-ply thick [$\pm$45] laminate to establish the development of macro-cracks until full two piece failure of the specimen.

4.2 Micro cracking and Initiation of Macro cracks

Two 16ply thick [±45] specimens were tested with the dimensions presented in the previous chapter (3.1). Testing of this material at quasi-static and intermediate rates showed very large displacements at two piece failure, for this reason the material was not expected to reach full failure within the duration of the SHTB test. While full failure would not be able to be reached the lower rate tests demonstrated a plateau region at low displacements, this plateau region showed the point at which energy began to be absorbed through macro-cracks leading up to ultimate failure. The SHTB was designed to produce enough displacement to reach this transition region, for this reason the material was chosen to show the importance of micro-crack formation at high rates.

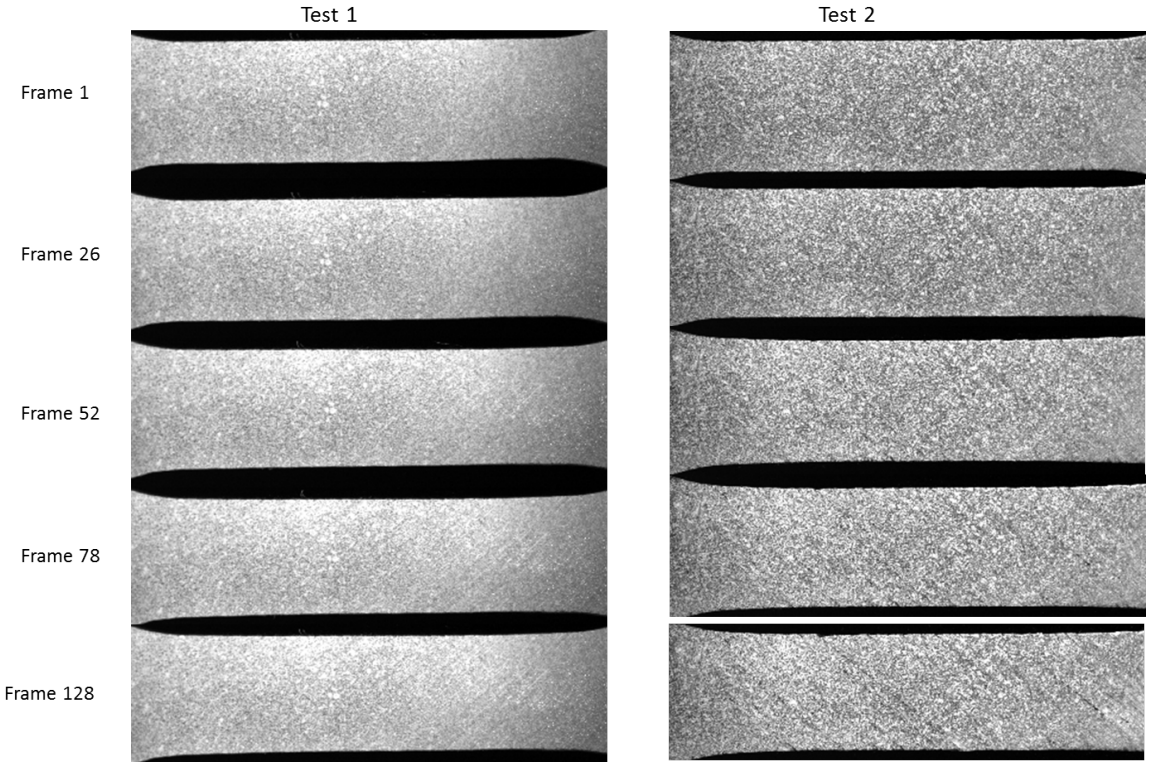

Figure 4.1: Damage observed in the first test specimen with CT scanning

The specimens were prepared with a thin speckle pattern created with only matte white

paint sprayed over the black surface of the carbon fiber laminate. This technique provided a strong enough contrast on the surface of the specimen to observe small cracks occurring on the specimen as well as a rough DIC correlation to gather strain data (4.1). The first test was conducted at 560psi and showed surface failure, this test was CT scanned to determine the extent of the damage(4.3). The second test was performed at 600psi to produce larger cracks throughout the specimen, this test showed much larger damage and reached a full two piece failure in compression after the duration of the test. Both tests showed a very similar stiffness trend along with a shear failure strain within 4% and a shear failure stress within 4% (**??**)

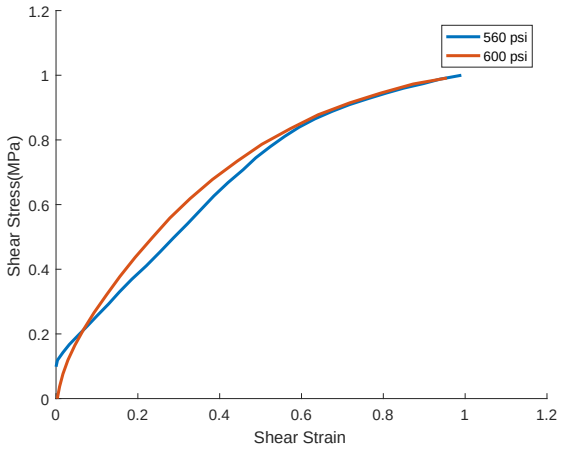

Figure 4.2: Comparison of Tested 16ply Thick Specimens

Test	Shear Strain	Shear Stress	Strain Rate
1	100	100	31.2
2	96.2	96.2	99.1
Average	98.1	99.5	58.3 height

Table 4.1: Normalized comparison of shear stress and shear strain failure values gathered through high rate testing of 16ply [±45] specimens

Using the strain measured using DIC analysis, with the failure strain taken to be the point at which the first visible crack appeared, a stress-strain plot was constructed for each test. Both tests showed strain concentration development in the along the fiber direction as the curves became non linear, as is expected. Macro-cracks became visible at the same point in each test resulting in the same final plotted strain.

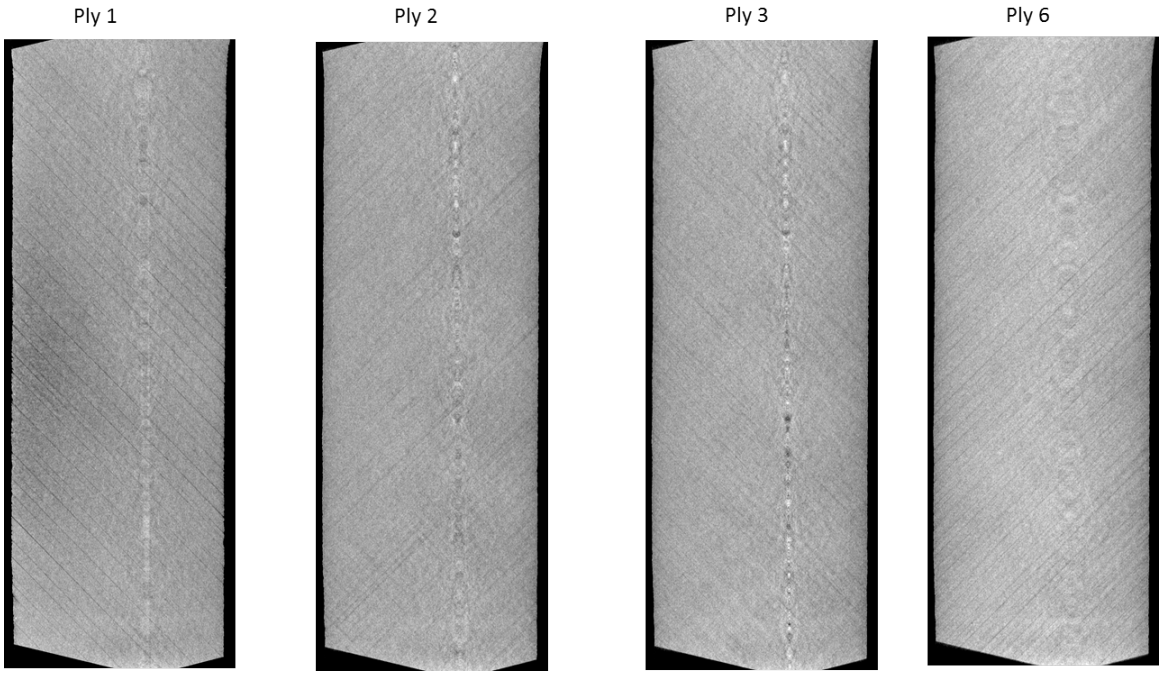

Figure 4.3: Damage observed in the first test specimen with CT scanning

4.3 Macro Crack Propagation and two piece failure

Testing of the [±45] material was continued with 8ply thick specimens, intended to reach full two piece failure within the duration of the test. The HPVX2 cameras offered a top end filming range of 5 million frames per second. In order to determine the largest possible amount of data three initial tests were completed to determine the maximum frame rate that would capture the full test event. Testing began at 250k pfs, then 500k pfs, and a third test was completed at 1 million fps and was not able to capture the full testing event. Three additional tests were completed and recorded at 500k fps. All the tests showed repeatable stiffnesses along with failure stresses and failure strains.

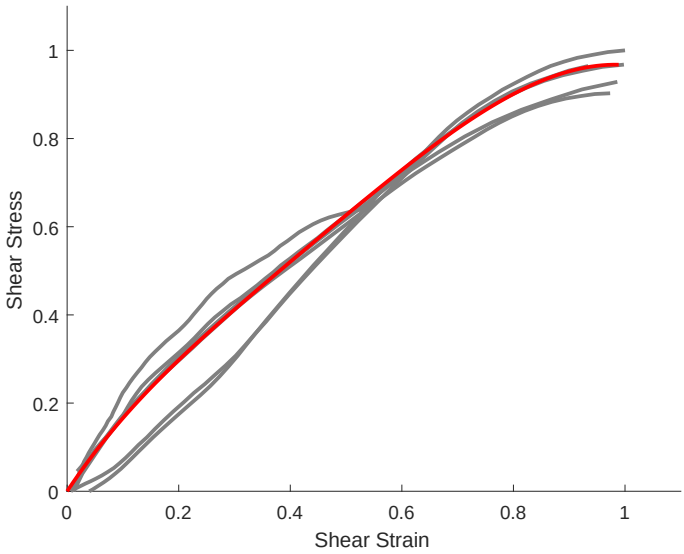

Figure 4.4: Comparison of Tested 8ply Thick Specimens

Test	Shear Strain	Shear Stress	Strain Rate
1	98.5	92.8	193
2	100	100	147
3	53.6	64.2	177
4	93.2	96.5	132
5	99.7	96.7	1938
6	97.1	90.2	102
Average	90.3	90	148
Standard Deviation	16.5	11.9	29.8

Table 4.2: Normalized comparison of shear stress and shear strain failure values gathered through high rate testing of 8ply [±45] specimens

The average shear failure strain across all six tests was found to be 90.3% of the highest recorded shear strain, while the average failure shear stress was 90% of the highest recorded value. These averages were slightly squed by test 3 (reftable:8ply45table). this test reached full failure within the duration of the pulse, however the camera was capturing the initiation of the loading at 1 million frames per second resulting on only part of the test being captured for post processing. Across the six tests a single master crack was observed to dictate the failure of the specimen, in two cases a second crack developed while the master crack was propagating. All six tests resulted in a full two piece failure with the characteristic chevron shape of this material.

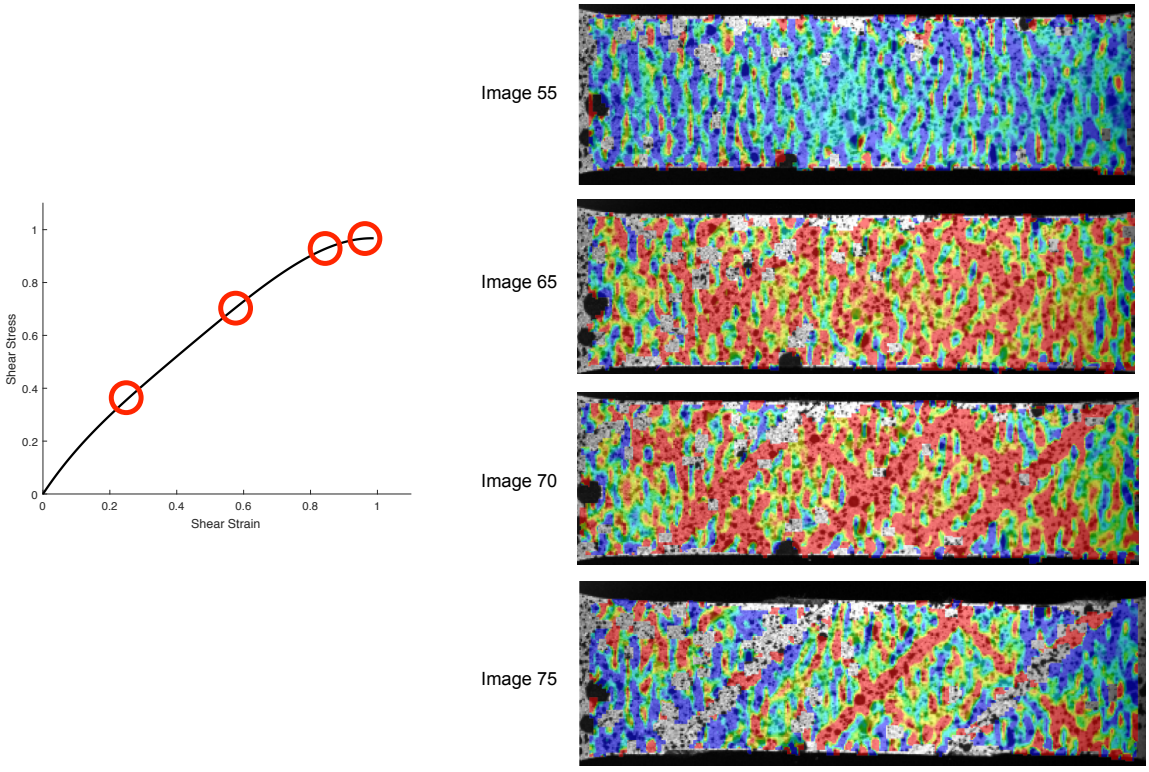

Figure 4.5: Representative curve with DIC strain localizations

4.4 Comparison of Results

Across all the laminate testing the failure stress, failure strains, and stiffnesses were very repeatable. Within the capabilities of the constructed SHTB no significant difference can be see in the effect of loading rate between 50 strain/sec and 360 strain/sec (**??**). Initial tests were conducted on small specimens designed off of the dimensions presented by Gilat, while later testing using the HPVX2 used scaled up dimensions of the same design and two different material thicknesses. Across the three specimen variations the gage section length provided a large variation in strain rate however only a 3.4% standard deviation was found in the failure stress and a 9.4% standard deviation in the failure stress.

Laminate	Shear Strain	Shear Stress	Strain Rate
8 ply	87.9	91.4	148
16 ply wide	100	100	58
16 ply thin	76.9	96	362
Average	88.3	95.8	189
Standard Deviation	9.4	3.4	127

Table 4.3: Normalized comparison of shear stress and shear strain failure values gathered through high rate testing of all tested laminate [±45] specimens

The higher frame rates of recording allowed for increased accuracy of data that agreed well with the lower recording frequency data. The higher frame rates also allowed for the creation of a visual strain field that showed strain localization due to micro-cracking, while the lower resolution and lower frame rate only allowed for an overall strain field to be constructed.

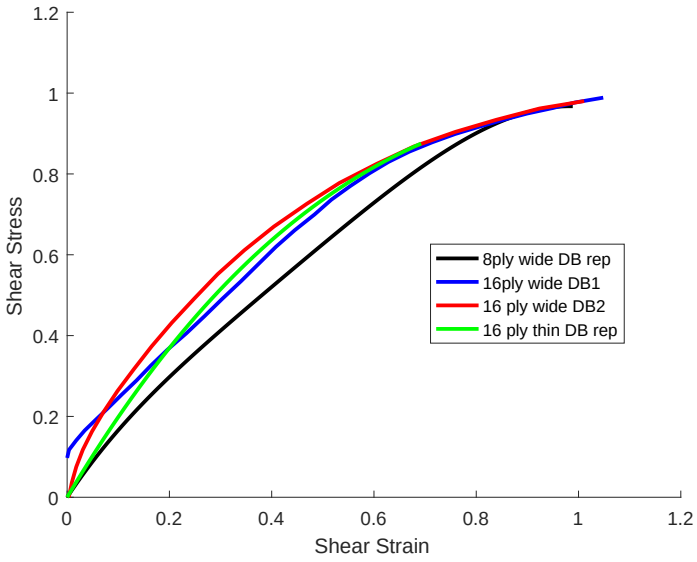

Figure 4.6: Comparison of Tested 16ply and 8ply Thick Specimens across all gage section dimensions

Chapter 5

DETERMINING SCHAPERY PARAMETERS

5.1 Introduction

In this section the Schapery theory will be introduced as a method to capture the pre-peak non-linearity in a model. The material testing and data processing methods used to gather the input parameters will then be presented.

5.2 Schapery Theory

When tested at quasi-static loading rates shear and transverse loading of composite laminates demonstrate a nonlinear behavior. This behavior is a result of matrix micro-cracking on the individual fiber and matrix length scale. Damage to the laminate is observed in the form of hackles, shear banding, micro fissures, fiber-matrix disband, as well as other forms Schapery theory utilizes a thermodynamically based work potential model to capture this behavior. The total work potential of the material, W_t, is comprised of the elastic potential W, and the dissipated potential, W_s. The dissipated potential is commonly represented by 'S' and only includes pre-peak dissipation. Damage occurring after the peak is regarded as macro-cracking and Schapery theory no longer applies.

$$W_t = W + S \tag{5.1}$$

W and S can be seen graphically in figure 5.1, The total work potential is stationary with respect to S, combining this assumption with 5.1 yields:

$$dW_t/ds = 0 \tag{5.2}$$

$$dW/dS = -1 \tag{5.3}$$

Classical Lamination Theory (CLT) allows the elastic potential to be written in the form

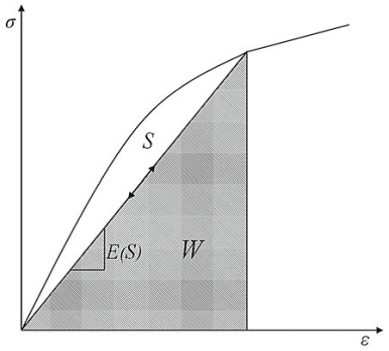

Figure 5.1: Schapery Theory Work Potential Schematic

$$W = \frac{1}{2}(E_{11}\epsilon_{11}^2 + E_{22}\epsilon_{22}^2 + G_{12}\gamma_{12}^2 + Q_{12}\epsilon_{11}\epsilon_{22}) \tag{5.4}$$

$$\text{where} \quad \nu_{12}\nu_{21} << 1 \tag{5.5}$$

The micro-damage only occurs in the matrix, this implies that the transverse and shear moduli, E_{22} and G_{12} are affected by the micro-damage while E_{11}, the longitudinal modulus, remains constant. The change in E_{22} and G_{12} is written in terms of micro-damage functions e_s(S) and g_s(S) shown in the equations below.

$$E_{22} = E_{22_0} e_s(S) \tag{5.6}$$

$$G_{12} = G_{12_0} g_s(S) \tag{5.7}$$

The pristine transverse and shear moduli are represented as E_{22_0} and G_{12_0} respectively. Assuming that $Q_{12} = \nu_{12}E_{22}$ is independent of S the evolution of micro-damage is found.

$$\frac{1}{2}(E_{22_0}\frac{de_s(S)}{dS}\epsilon_{22}^2 + G_{12_0}\frac{dg_s(S)}{dS}\gamma_{12}^2) = -1 \tag{5.8}$$

It has been shown, [2], that the applied strain, ϵ_x in the experimental coordinate, varies in a cubic relation to S, ϵ_x^3, A direct relation is achieved by introducing a reduced damage coefficient, S_r

$$S_r = sqrt[3]S \tag{5.9}$$

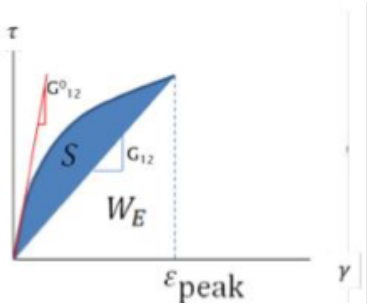

Figure 5.2: Shear stress v. Shear strain, G_{12} and S_{12} calculations

Plugging the reduced damage coefficient into equation 5.8 produces:

$$\frac{1}{2}(E_{22_0}\frac{de_s(S_r)}{dS_r}\epsilon_{22}^2 + G_{12_0}\frac{dg_s(S_r)}{dS_r}\gamma_{12}^2) = -3S_r^2 \tag{5.10}$$

5.3 Calculation of Micro-damage functions

The Schapery micro-damage functions, e_s(S) and g_s(S) are determined through mechanical testing of angle ply laminates. The shear micro-damage function, g_s(S), is determined through testing of $[^{\pm}45]_s$ laminates. The transverse micro-damage function in tension, e_{st}(S), is determined through the testing of 15^o off axis laminates.

5.3.1 Shear Micro-damage Calculation

Testing of $[^{\pm}45]_s$ laminates provide loading direction stress and strain data, as well as strain data in the transverse direction. Using these data shear stress and shear strain is calculated using equation 5.11 and 5.12 below. The resultant shear data is then used to produce a shear stress v. shear strain plot for each test.

$$\tau_{12} = \frac{\sigma_{xx}}{2} \tag{5.11}$$

$$\gamma_{12} = \epsilon_{xx} - \epsilon_{yy} \tag{5.12}$$

By drawing a secant stiffness at each point along the shear stress v. shear strain curve produces a G_{12} data point. Integrating between the representative curve and the secant

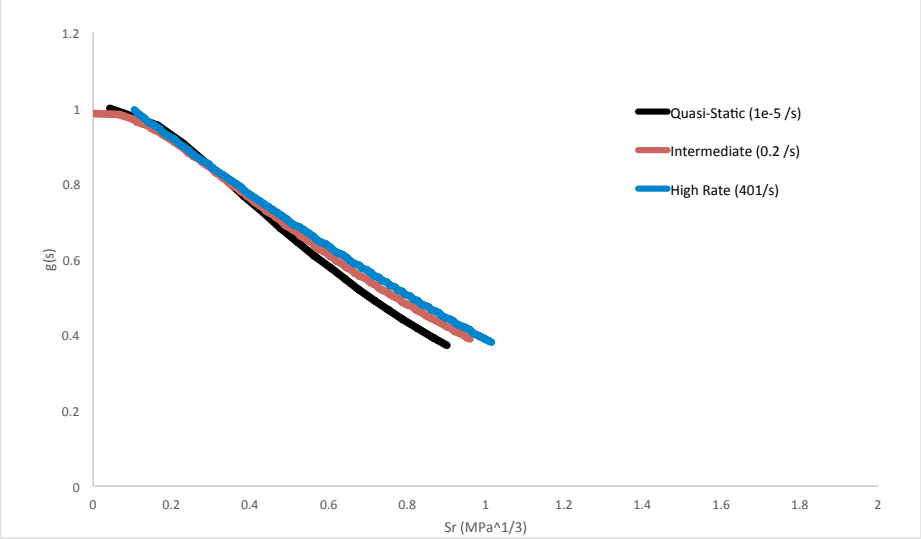

Figure 5.3: Shear micro-damage functions

stiffness line produces the energy absorption coefficient S_{12}. The initial data points collected during testing produce a virtual stiffness that is not characteristic of the material. These points are eliminated due to the inaccuracy, leaving the truncated data set that is a more accurate representation of the material response, this process is discussed in more detail in the following chapter. The reduced energy absorption coefficient is then calculated ($S_r^{\frac{1}{3}}$) and plotted against G_{12}/G_{12_0}, producing the shear micro-damage parameter curve g(s). These data points are then fitted with a fifth order polynomial, the coefficients of which will be used as input parameters for the modeling discussed in the following chapter

The resultant micro-damage curves illustrate the minimally increasing effect of micro-damage on the material as the applied strain rate is increased. Quasi-static loading rates allow the specimen to shift and adjust incrementally throughout the duration of the test leading to more energy absorption and corresponding micro-cracking before failure. As the loading rate increases the material becomes stiffer and micro-cracks form earlier in the test leading to a more linear micro-damage function. This trend is shown both by the increased shear stiffness (G_{12}) from low to high rates, and the increasing linearity of the g(s) curves.

5.3.2 Transverse Micro-damage Calculation

The transverse micro-damage function in compression as demonstrated by Sicking [2] is determined from the results of $[\pm 30]_s$ laminates. this laminate was suggested as a material system that provides a larger strain than higher angle laminates, thus allowing it to absorb more work and prove a good relationship between E_{22} and S.

$$\begin{bmatrix} \epsilon_{11} \\ \epsilon_{22} \\ \gamma_{12} \end{bmatrix} = \begin{bmatrix} c^2 & s^2 & cs \\ s^2 & c^2 & -cs \\ -2cs & 2cs & c^2 - s^2 \end{bmatrix} \begin{bmatrix} \epsilon_{xx} \\ \epsilon_{yy} \\ \gamma_{xy} \end{bmatrix} \tag{5.13}$$

$$\tau_{12} = G_{12_0} g(S) \gamma_{12} \tag{5.14}$$

$$S_{total} - S_{12} = S_{22} \tag{5.15}$$

Tensile testing of the $[\pm 30]_s$ laminate provides a global stress v. strain relation (**??**) from which a representative laminate level axial stress v. axial strain curve is constructed. Using Schapery's theory a secant curve representing G_{12} is drawn from every stress point(5.3.1). Integrating between the curve and the secant line produces the total energy absorption of the system 'S_{total}'. The measured strains (ϵ_{xx},ϵ_{yy},γ_{xy}) are then rotated into the lamina co-ordinate system (5.13), providing the local axial, transverse, and shear strains (ϵ_{11},ϵ_{22},γ_{12}). The lamina level shear strains are then substituted into 5.14, producing the lamina level shear stresses (τ_{12}) at each strain point. the lamina level shear stress v. shear strain curve is then constructed and used to calculate the shear micro-damage variable S_{12}. As there are two modes of energy absorption occurring in the specimen, and the shear response relationship (5.14) is known, the transverse micro-damage variable can be determine through the relationship in 5.15.

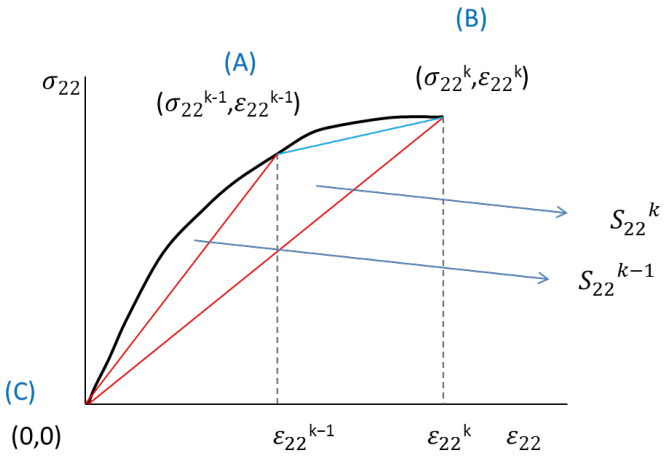

Figure 5.4: Incremental analysis

Using the variables calculated directly form the test data (τ_{12},ϵ_{11},ϵ_{22},γ_{12},S_{total},S_{12},S_{22}) a closed form solution can be used to solve for the transverse stiffness $E_2 2$ and to determine the transverse micro-damage function in compression $e(S_c)$ in an incremental fashion (figure 5.3.2).

The incremental solution used to evaluate these data starts with an initial point (A) and triangulates the following point on the lamina level transverse stress v. transverse strain curve (B). The first two points of the triangle are known, the initial loading point of the curve and the origin (C). Both the stress and strain values are known at these two points from the test data and subsequent analysis. The third point is the next loading point where only the strain value is known. The transverse stress at this second loading point is calculated by finding the difference in area between the two energies dissipated due to shear and transverse compression. Taking the difference between S at the initial point and S at the second point results in the change in energy, δS. This change in energy represents the difference in area between the two incremental energies. The difference in area can be equated to the area of the triangle created between the origin and the two load curve values. The area of the triangle is a function of E_{22}, allowing the transverse stiffness value to be the only unknown. Solving the equation produces the transverse stiffness evolution.

$$\begin{bmatrix} \theta_{11} \\ \theta_{22} \\ \tau_{12} \end{bmatrix} = [Q] \begin{bmatrix} \epsilon_{11} \\ \epsilon_{22} \\ \gamma_{12} \end{bmatrix} \tag{5.16}$$

$$\text{where [Q]} = \begin{bmatrix} Q_{11} & Q_{12} & 0 \\ Q_{12} & Q22 & 0 \\ 0 & 0 & Q_{66} \end{bmatrix} \tag{5.17}$$

$$Q_{11}=\frac{E_1}{1-\nu_{12}\nu_{21}} \quad Q_{12}=\frac{\nu_{12}E_2}{1-\nu_{12}\nu_{21}} \quad Q_{22} = \frac{E_2}{1-\nu_{12}\nu21}$$

$$Q_{66}=G_{12} \quad \nu_{21}=\frac{\nu12E_2}{E_1}$$

$$Q_{22}^k=Q_{22}^{k-1}\epsilon_{22}^k \text{ - } 2\Delta \text{ S}/\epsilon_{22}^{k-1}$$

where k is the solved point and (k-1) is the following point on the curve.

Using the method discussed above the quasi-static and intermediate rate testing data was analyzed to determine the transverse micro-damage functions in compression. The Schapery parameter analysis of the quasi-static rate tests show a softening trend in both the shear and transverse moduli due to the formation of micro cracks. The intermediate rate shows a similar but slightly more linear global response and the structural analysis of the local response shows that the shear modulus degradation is the dominant mode of energy dissipation. The transverse modulus degradation is much lower than that of the quasi-static loading case, (figures 5.5, 5.6)

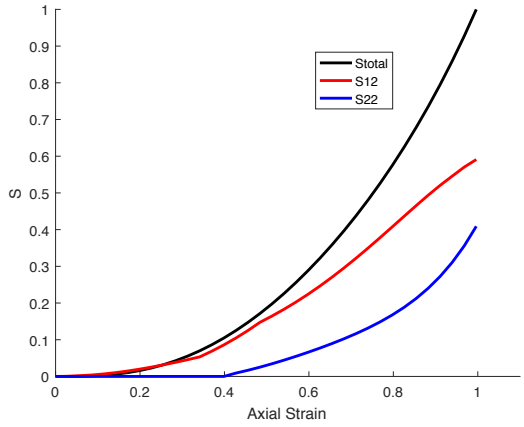

Figure 5.5: Micro-damage energy functions v. global axial strain of Quasi-static rate tests

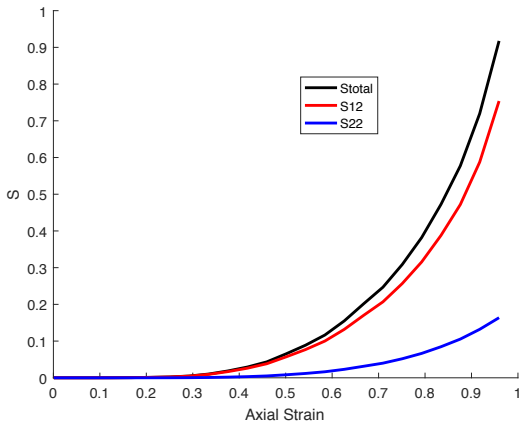

Figure 5.6: Micro-damage energy functions v. global axial strain of Intermediate rate tests

As the loading rate increased the material was restricted from adjusting to the load, this in turn restricted the rotation of the fibers, causing shear micro damage to dominate failure at higher loading rates. At lower loading rates the material was allowed time to adjust and thus the fibers could rotate, resulting in the transverse compression being the dominate mode of failure. The energy absorption due to compression is then plotted against the stiffness degradation (figure 5.3.2) to produce $e(S_c)$ curves for the quasi-static and intermediate loading rates respectively.

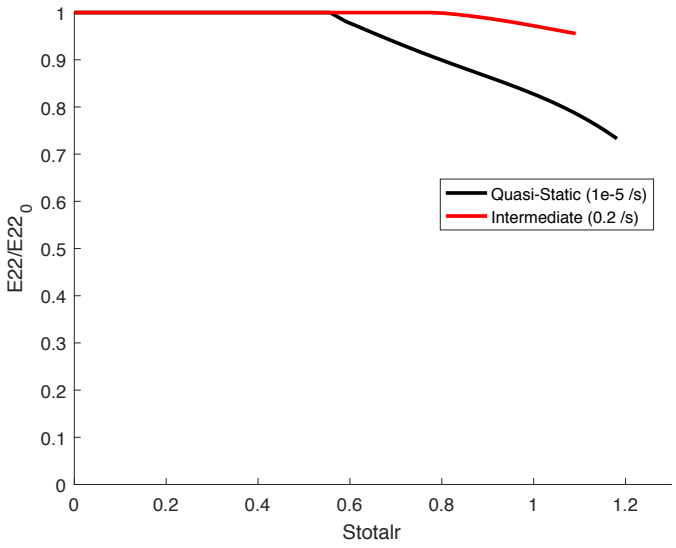

Figure 5.7: Transverse micro-damage functions, E_{22}/E_{220} v. S_{total} in compression

The transverse micro-damage functions in tension were determined using a [+15] unidirectional laminate. Analysis of the test data was completed using the same closed form solution method dicussed for the transverse micro-damage function in compression with the [±30] laminates. Because the [+15] laminates are unidirectional the global shear strain (γ_{xy} is no longer assumed to be zero as in a cross-ply. However after closely analyzing the test results (5.3.2) at each rate it was determined that the fixed gripping conditions imposed on the specimens did not allow for shear strain to occur. Thus, for the following analysis the global shear strain was assumed to be zero.

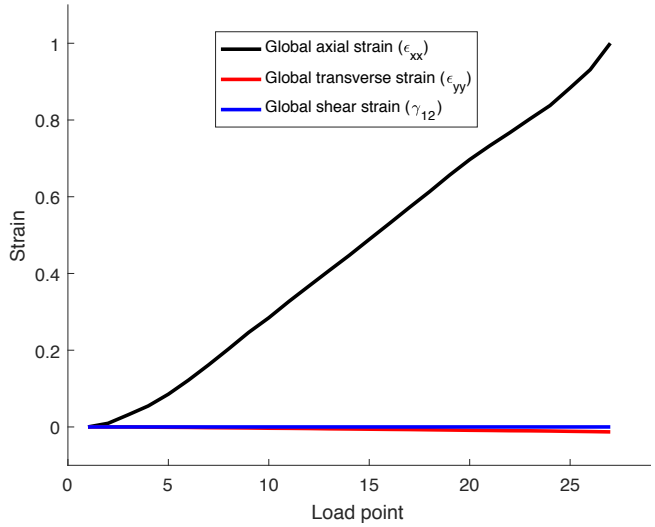

Figure 5.8: Global shear strains measured on [+15] unidirectional specimen

Testing of the [+15] unidirectional laminates showed that as the applied strain rate increased the material exhibited a softening trend. Plotting the transverse micro-damage variable (S_{22}) against teh transverse stiffness (E_{22}) shows and increased sensitivity to micro damage as the applied loading rate is increased. Quasi-static loading rates allowed for a large amount of micro-damage to occur, throughout the duration of the test with a decrease in E_{22} that is small relative to the intermediate rate testing. Intermediate rate testing allowed for similar micro-damage accumulation as the quasi-static testing, with a large degradation in E_{22}. High rate testing exhibited a much stiffer response than the lower strain rates, this is shown by how little micro-damage (0.23 S_{22r}) is accumulated in the specimen at failure. The small micro damage accumulation in the high rate testing was coupled with a small E_{22} degradation, this behavior follows the abrupt failure with only macro cracking seen in testing.

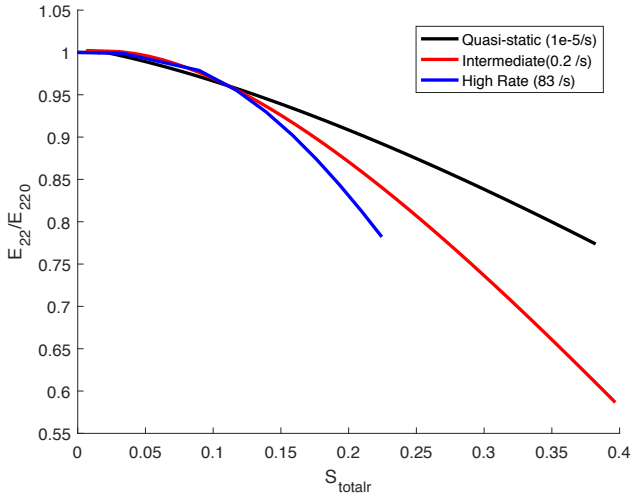

Figure 5.9: Transverse micro-damage functions in tension

Chapter 6

APPLICATION OF MEASURED MATERIAL CHARACTERISTICS TO A PREDICTIVE MODEL

6.1 Introduction

In the previous chapter Schapery theory was discussed as a method to model the pre-peak non-linearity due to matrix micro-cracking. In order to capture the post peak behavior of the material it is necessary to use a second model in addition to Schapery theory. A Crack Band model ([3])has previously been used in conjunction with Schapery theory to model this behavior ([4]). Crack Band captures the post-peak behavior of the material by tracking the damage, and failure due to matrix transverse and shear cracking in tension and compression, as well as fiber failure in tension and compression. Crack Band was thus used to 'Extend' Schapery theory, providing EST. The remainder of this chapter will provide a brief introduction to the Crack Band theory. The capabilities of the method will then be illustrated by modeling three different Open Hole Tension laminates at intermediate strain rates, using the test data presented in chapter 4.

6.2 Crack Band, Extended Schapery Theory (EST)

The energy density equation presented in 5.1 is updated to include the added modes of failure captured by crack band:

$$W_t = W_E + S + S_I^m + S_{II}^m + S_1^f \tag{6.1}$$

In this equation W_e is the elastic energy, S is the dissipated energy due to micro cracking, from Schapery theory, S_I^m and S_I^m and S_{II}^m are the dissipated energy due to mode I and mode II matrix cracking, and S_I^f is the dissipated energy due to fiber breakage/rupture. The stationary principle (5.2,5.3)for each internal state variable provides:

$$\frac{\delta W_E}{\delta S} = -1 \tag{6.2}$$

$$\frac{\delta W_E}{\delta S_I^m} = -1 \tag{6.3}$$

$$\frac{\delta W_E}{\delta S_{II}^m} = -1 \tag{6.4}$$

$$\frac{\delta W_E}{\delta S_I^f} = -1 \tag{6.5}$$

Failure and damage caused my macroscopic cracking is represented using the Hashin-Rotem failure criterion.

$$\frac{{\epsilon_{22}}^2}{\gamma_T} + \frac{{\gamma_{12}}^2}{Z} = 1 \qquad \epsilon_{22} \geq 0 \tag{6.6}$$

$$\frac{{\epsilon_{22}}^2}{\gamma_C} + \frac{{\gamma_{12}}^2}{Z} = 1 \qquad \epsilon_{22} < 0 \tag{6.7}$$

In the equations above, Y_T and Y_C are the lamina transverse direction failure strain in tension and compression and the shear failure strain is represented by 'Z'. The fiber direction failure/damage initiation criteria are represented similarly:

$$\frac{{\epsilon_{11}}^2}{X_T} = 1 \qquad \epsilon_{11} \geq 0 \tag{6.8}$$

$$\frac{{\epsilon_{11}}^2}{X_C} = 1 \qquad \epsilon_{11} \geq 0 \tag{6.9}$$

Where X_T and X_C are the lamina fiber direction failure strains in tension and compression.

The transition from Schapery theory to Crack Band occurs when an element transitions from and element with micro-cracking to an element with macro-cracking. This transition preserves the micro-cracking parameter 'S' at a fixed value. The macro-cracked element then follows the traction separation law. This transition also represents a change from

continuum damage modeling governed by stress and strain to a non-continuum modeling approach governed by discrete traction separation laws for each mode of failure.

Pineda and Waas derived the energy potentials associated with each mode of crack opening([4]). The equations account for both the total energy available for dissipation and a subtraction of the recoverable energy if the crack is closed. The energy potential equations are then:

$$S_1^m = \frac{G_I^m}{l_e^\theta} - \frac{t_I^m \delta_I^m}{2 l_e^\theta} \tag{6.10}$$

$$S_{II}^m = \frac{G_{II}^m}{l_e^\theta} - \frac{t_{II}^m \delta_{II}^m}{2 l_e^\theta} \tag{6.11}$$

$$S_I^f = \frac{G_I^f}{l_e^{\theta+90}} - \frac{t_I^f \delta_I^f}{2 l_e^{\theta+90}} \tag{6.12}$$

In the equations above the subscripts I and II refer to mode I and mode II cracks, superscripts m and f refer to the matrix and fiber failure directions, G represents the fracture toughness, t and δ represent traction and separation. The crack length depends on the crack direction, in the transverse and shear directions the crack will grow in the fiber direction, this is l_e^θ where θ is the fiber direction. In the case of fiver breakage the crack will grow perpendicular to the fiber direction and the element length is given by $l_e^{\theta+90}$. It is important to note that the last three energy potentials are only the elastic strain energy of the crack, this allows the tractions to be related to the secant stiffness and displacement in the traction separation laws.

$$t_I^m = k_I^m \delta_I^m \tag{6.13}$$

$$t_{II}^m = k_{II}^m \delta_{II}^m \tag{6.14}$$

$$t_I^f = k_I^f \delta_I^f \tag{6.15}$$

K is the secant stiffness associated with the matrix direction mode I and II crack, and the mode I crack in the fiber direction. Expressing the secant stiffness as a function of energy potentials it is possible to determine the elastic strain energy of the crack.

$$W_I^m = \frac{k_I^m(S_l^m)\delta_I^{m^2}}{2l_e^\theta} \tag{6.16}$$

$$W_I^m = \frac{k_{II}^m(S_{lI}^m)\delta_{II}^{m^2}}{2l_e^\theta} \tag{6.17}$$

$$W_I^f = \frac{k_I^f(S_l^f)\delta_I^{f^2}}{2l_e^{\theta+90}} \tag{6.18}$$

The total elastic strain energy density can then be expressed as:

$$W = \frac{1}{2}(E_{11}\epsilon_{11}^2+E_{22}\epsilon_{22}^2+G_{12}\gamma_{12}^2)+Q_{12}\epsilon_{11}\epsilon_{22}+\frac{k_l^m(s_l^m)\delta_l^{m^2}}{2l_e^\theta}+\frac{k_{II}^m(s_I^m l)\delta_{II}^{m^2}}{2l_e^{\theta+90}}+\frac{k_l^f(s_l^f)\delta_l^{f^2}}{2l_e^{\theta+90}} \tag{6.19}$$

Inserting equations 6.2,6.3 ,6.4 , and 6.5 to 6.19 produces the Internal State Variable (ISV) evolution equations,

$$\frac{1}{2}(E_{220}\frac{de_s(S_r)}{dS_r}\epsilon_{22}^2 + G_{120}\frac{dg_s(S_r)}{dS_r}) = -3S_r^2 \tag{6.20}$$

$$\frac{1}{2l_e^\theta}\frac{dk_l^m}{dS_l^m}\delta_l^{m^2} = -1 \tag{6.21}$$

$$\frac{1}{2l_e^\theta}\frac{dk_{lI}^m}{dS_{Il}^m}\delta_{Il}^{m^2} = -1 \tag{6.22}$$

$$\frac{1}{2l_e^{\theta+90}}\frac{dk_l^f}{dS_l^f}\delta_l^{f^2} = -1 \tag{6.23}$$

Equations 6.21 is the same equation as 5.10 from Schapery theory. The matrix mode I and II failures are coupled using a first order power law mixed mode criteria. The energy potentials (S_I^m,$S_I^m I$,S_I^f) are then evaluated using equations, 6.20, 6.21,and 6.22 at the initiation of failure in terms of applied strain using the traction separation laws and kinematics. The traction are then critical cohesive strengths, providing the traction law secant stiffnesses.

$$k_l^m = -\int \frac{t_{IC}^m}{\delta_l^{m^2}} d\delta_l^m \tag{6.24}$$

$$k_{II}^{m} = -\int \frac{t_{IIC}^{m}}{\delta_{Il}^{m^2}} d\delta_{Il}^{m} \tag{6.25}$$

$$k_{I}^{f} = -\int \frac{t_{IC}^{f}}{\delta_{I}^{f^2}} d\delta_{l}^{f} \tag{6.26}$$

$$notingthat \frac{dS_{l}^{m}}{d\delta_{l}^{m}} = \frac{t_{I}^{m} C}{2l_{e}^{\theta}} \quad , \quad \frac{dS_{II}^{m}}{d\delta_{II}^{m}} = \frac{t_{IIC}^{m}}{2l_{e}^{\theta}} \quad , \quad \frac{dS_{I}^{f}}{d\delta_{I}^{f}} = \frac{t_{IC}^{f}}{2l_{e}^{\theta+90}} \tag{6.27}$$

Maintaining a secant stiffness 'k' value of zero and evaluating the integrals when the critical separations of the traction separation laws are achieved results in the equations for secant stiffness in terms of the separations.

$$k_{I}^{m} = t_{IC}^{m}(\frac{1}{\delta_{l}^{m}} - \frac{t_{IC}^{m}}{2G_{IC}^{m}}) \tag{6.28}$$

$$k_{II}^{m} = t_{IIC}^{m}(\frac{1}{\delta_{II}^{m}} - \frac{t_{IIC}^{m}}{2G_{IIC}^{m}}) \tag{6.29}$$

$$k_{I}^{f} = t_{IC}^{m}(\frac{1}{\delta_{l}^{f}} - \frac{t_{IC}^{f}}{2G_{IC}^{f}}) \tag{6.30}$$

Where G_{IC}^{m} and G_{IIC}^{m} are the mode I and mode II fracture toughnesses of the matrix and G_{IC}^{f} is the mode I fracture toughness of the fiber direction.

The strains in the post-peak regime are related to the traction separation by,

$$l_{e}^{\theta+90}\epsilon_{11} = l_{e}^{\theta+90}\epsilon_{11}^{c} + \delta_{I}^{f} \tag{6.31}$$

$$l_{e}^{\theta}\epsilon_{22} = l_{e}^{\theta}\epsilon_{22}^{c} + \delta_{I}^{m} \tag{6.32}$$

$$l_{e}^{\theta}\gamma_{12} = l_{e}^{\theta}\gamma_{12}^{c} + 2\delta_{II}^{m} \tag{6.33}$$

ϵ_{11}^{c}, ϵ_{22}^{c}, and γ_{12}^{c} are the strains in the longitudinal direction, transverse direction and shear direction respectively. The tangent stiffness is then obtained as a function of global strain,

$$k_{I}^{m} = t_{IC}^{m}\left[\frac{1}{l_{e}^{\theta}(\epsilon_{22} - \epsilon_{22}^{c})} - \frac{t_{IC}^{m}}{2G_{IC}^{m}}\right] \tag{6.34}$$

$$k_{II}^{m} = t_{IIC}^{m}\left[\frac{1}{l_e^{\theta}(\gamma_{12}-\gamma_{12}^{c})} - \frac{t_{IIC}^{m}}{2G_{IIC}^{m}}\right] \tag{6.35}$$

$$k_{I}^{f} = t_{IC}^{f}\left[\frac{1}{l_e^{\theta+90}(\epsilon_{11}-\epsilon_{11}^{c})} - \frac{t_{IC}^{f}}{2G_{IC}^{f}}\right] \tag{6.36}$$

Finally the longitudinal, transverse and shear moduli of the element can be calculated in terms of the strains.

$$E_{11} = \left[\frac{1}{e_{110}} - \frac{\epsilon_{11}-\epsilon_{11}^{C}}{t_{IC}^{f}(1+\frac{l_e^{\theta+90}t_{IC}^{f}}{2G_{IC}^{f}}(\epsilon_{11}-\epsilon_{11}^{C}))}\right]^{-1} \tag{6.37}$$

$$E_{22} = \left[\frac{1}{e_{22}^{*}} - \frac{\epsilon_{22}-\epsilon_{22}^{C}}{t_{IC}^{m}(1+\frac{l^{\theta_e}t_{IC}^{m}}{2G_{IC}^{m}}(\epsilon_{22}-\epsilon_{22}^{C}))}\right]^{-1} \tag{6.38}$$

$$G_{12} = \left[\frac{1}{G_{12}^{*}} - \frac{\gamma_{12}-\gamma_{12}^{C}}{2t_{IIC}^{m}(1+\frac{l^{\theta_e}t_{IIC}^{m}}{4G_{IIC}^{m}}(\gamma_{12}-\gamma_{12}^{C}))}\right]^{-1} \tag{6.39}$$

E_{22}^{*} and G_{12}^{*} represent the degraded transverse and shear moduli due to micro-damage, these are drawn from Schapery theory. One final element size is implemented to ensure snap-back behavior does not occur.

$$l_e^{\theta+90} < \frac{2G_{IC}^{f}E_{11}}{t_{IC}^{f2}} \tag{6.40}$$

$$l_e^{\theta} < min\Big\{\frac{2G_{IC}^{m}E_{11}^{*}}{t_{IC}^{m2}}, \frac{2G_{IIC}^{m}G_{12}^{*}}{t_{IIC}^{m2}}\Big\} \tag{6.41}$$

6.3 Prediction of Open Hole Tension specimens failures at intermediate loading rates

In order to verify the validity of the rate dependent test results gathered in chapter 4 EST was implemented in a predictive model of thee Open Hole Tension specimens constructed of the same lamina and matrix material used in the rate testing. The specimens were modeled in three layups, 'soft', 'quasi', and 'hard' laminates. Due to the limitations of our testing frame (for validation purposes) and the fact that high rate test results were

not successful in achieving full two piece failure, only intermediate and quasi-static strain rates were modeled. The modeling results would then be used both to determine if OHT coupons would demonstrate rate dependent strength characteristics and as a prediction of how at rate testing would behave. The soft laminate was constructed of a [10/80/10] layup of 0^0,45^0, and 90^0 lamina respectively. The quasi laminate was a [25/50/25] layup, and the hard laminate consisted of a [50/40/10] percent lamina stacking. Each of these three layups were modeled using a single shell EST model and the input properties gathered in chapter 4. Quasi-static tests were modeled using standard steps, while intermediate rate models were created using mass scaling to achieve the 0.2 strain/sec.

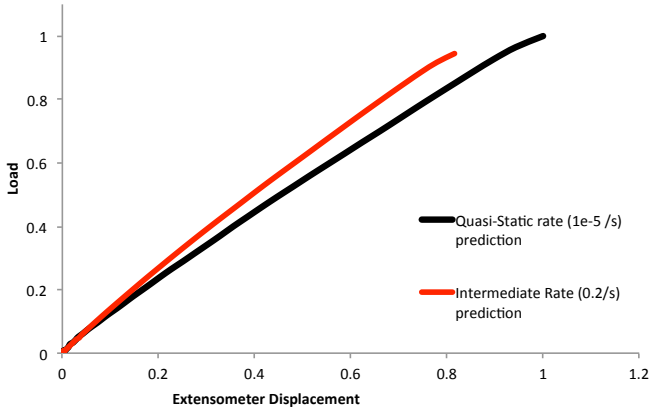

Figure 6.1: Predictive EST model results of Soft laminate for Quasi-Static and Intermediate strain rates

	Failure Load (%)	Failure Displacement(%)
Quasi-Static	100	100
Intermediate	94.6	81.3

Table 6.1: Predictive model failure values of Soft laminate

Laminate	Ply angle	SDV	QS Failure Stage	IR Failure Stage
Soft	45	14	76	70
		19	54	70
	0	14	60	56
		19	50	17
	90	14	54	56
		19	35	17

Table 6.2: Solution Dependent Variable Failure Comparison of Soft Laminate

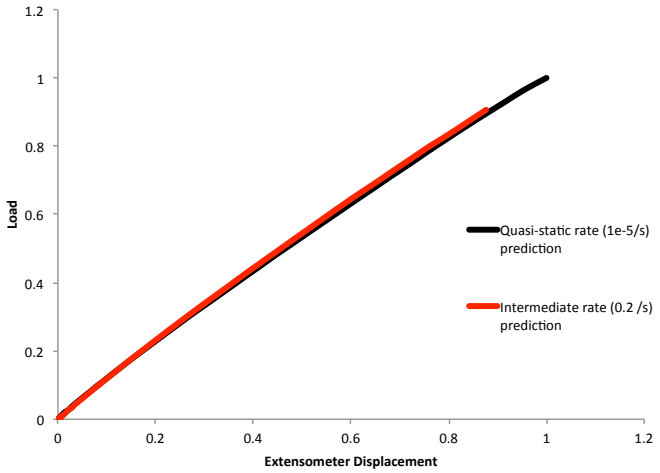

Figure 6.2: Predictive EST model results of Quasi laminate for Quasi-Static and Intermediate strain rates

	Failure Load (%)	Failure Displacement(%)
Quasi-Static	100	100
Intermediate	90.6	87.5

Table 6.3: Predictive model failure values of Quasi laminate

Laminate	Ply angle	SDV	QS Failure Stage	IR Failure Stage
Quasi	45	14	65	52
		19	40	11
	0	14	54	44
		19	54	13
	90	14	63	53
		19	32	13

Table 6.4: Solution Dependent Variable Failure Comparison of Quasi Laminate

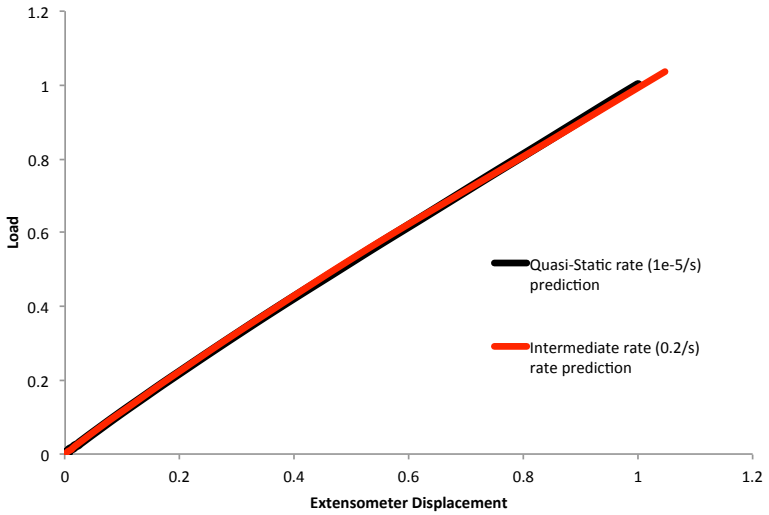

Figure 6.3: Predictive EST model results of Hard laminate for Quasi-Static and Intermediate strain rates

	Failure Load (%)	Failure Displacement(%)
Quasi-Static	100	100
Intermediate	103.6	103.2

Table 6.5: Predictive model failure values of Hard laminate

Laminate	Ply angle	SDV	QS Failure Stage	IR Failure Stage
Hard	45	14	54	49
		19	34	10
	0	14	50	46
		19	50	11
	90	14	51	48
		19	31	11

Table 6.6: Solution Dependent Variable Failure Comparison of Hard Laminate

The modeling results of each of the three laminates showed that the soft laminate stiffness experienced the largest change in stiffness. The intermediate rate failure displacement was expected to be 79.5% lower and a failure load 5.4% lower than the quasi-static model respectively. The quasi and hard laminates showed a slight stiffening, however the stiffness was not predicted to be outside the experimental variance of either rate. The quasi laminate predicted a 13% lower failure displacement and a 10% lower failure load, while the hard laminate predicted a 3% higher failure displacement and a 3% higher failure load. EST performs most if its conditional analysis based on the relationship of Solution Dependent Variables(SDVs). These values can be output to monitor locations in the model where damage occurs and at what stage of the loading. The three values that were most closely considered during this testing were those linked to Schapery theory input parameters, axial fiber failure (SDV14), transverse failure (SDV18) and shear failure (SDV19). The shear and transverse failure criteria were observed to be triggered at the same stage across all tests, to keep it simple only one of these values was presented(6.3,6.3,6.3). Across all tests failure was first observed in the 90^0 plys followed by the 45^0plys and finally the 0^0plys. Additionally it was consistently shown that the failures were initiated earlier in the loading curve as the applied strain rate increased. This follows the stiffening trend what is expected as the input parameters and previous testing had demonstrated. It was established that some rate dependance was displayed by the three laminates at different degrees. These predictive models were then validated with testing of OHT specimens at intermediate loading rates.

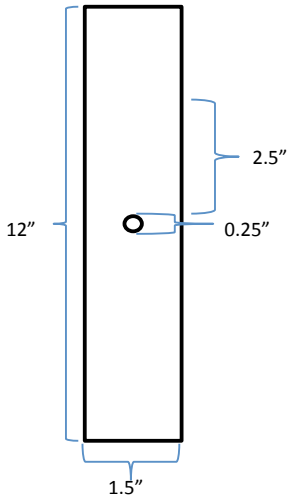

Figure 6.4: Dimensions of OHT specimens

6.4 Validation testing of OHT coupons

The OHT prediction models discussed in the previous section were validated with testing of physical specimens. The predictive models determined that a different response was observed at an increased strain rate, thus testing was only conducted at the intermediate strain rate for validation. The specimens were dimensioned according to ASTM OHT testing standard, and the tests were conducted on a Shore Western hydraulically actuated load frame with hydraulic wedge grips and a 35,000 lb capacity. The load was recorded using a model 1020ACK-25K-B modified interface load cell that is capable of measuring very load loads as well as high. Displacement fields were measured using DIC analysis of a painted speckle pattern around the hole on the surface of the test specimen.

Five OHT specimens of each layup (soft, quasi, hard) were cut according to ASTM standard D3039/D3039M. This standard requires that the specimen width (w) to hold diameter (d) can be no less than 6. Additionally it is necessary that the hole diameter is no smaller than 0.25 inches to ensure that plan stress assumptions can be applied to the laminate (taking into consideration the specimen thickness). The Shore Western load frame uses grips that accept a maximum specimen width of 1.5”. Accounting for the limitations

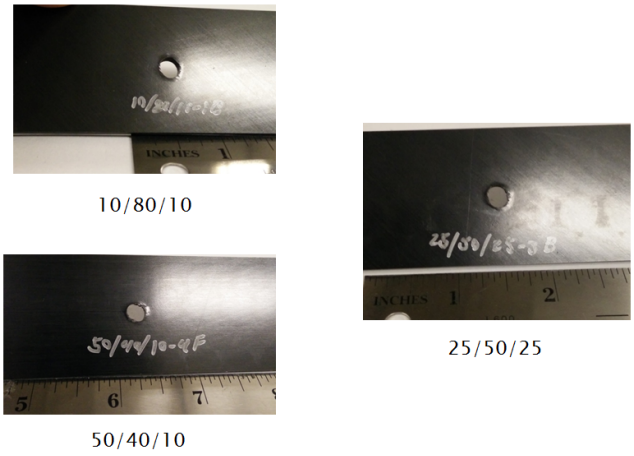

Figure 6.5: Delaminations observed on back side of received specimens

and standards it was determined that a 1.5" wide, 12" long specimen with a 5" gage section and a 0.25" diameter centered hole would allow allow for the necessary 0.2 strain/sec applied strain rate (figure 6.4).

It is important to note that the specimens were prepared by a separate company and the drilling of the center holes was not performed cleanly. As a result the specimens were received with significant delamination on whichever side was facing down during the drilling 6.4. The testing process was continued under the assumption that the imperfections would only have a small effect on the results.

Test specimens were prepared in two ways, the hard laminates were tabbed with tapered glass fiber tabs the same thickness as the specimen, while the quasi and soft panels were tabbed with emory cloth. The hard laminate was fabricated with 90^0 plys on the surface, this can cause slipping in the grips, the slipping is avoided through tabbing. The quasi and soft specimens were fabricated with 45^0 plys on the surface which can sustain a much larger load. Once the tabs were added a black and white speckle pattern was applied to the gage section of the specimens. Initially one specimen form each laminate was tested at a rate of 0.5 in/sec. The results of this initial test determined if a difference could be observed in the applied loading rate and the the rate experienced between the laminates. The initial tests

showed measured strain rates of 0.6 /s, 0.6 /s, and 0.5/s, indicating that all the laminates could be loaded at the same applied load rate on the load frame. The remaining four specimens of each laminate were tested at the maximum actuator displacement rate of 1.5 in/sec. At this applied rate the resultant strain rates experienced by the specimens falls in the same range as the 'intermediate rate' testing presented in the previous chapter (0.2 /sec). This allowed for a direct comparison of the test results to the EST predictive analysis.

Testing was conducted starting with the hard laminate then progressing down in stiffness to the quasi then soft laminates. The hard laminate testing showed consistent stiffness trends across all five tests with a small failure load variance of 4.2% and a failure displacement variance 0f 1.9%. The average failure load was found to be 9% higher than predicted by the EST model and the average failure displacement was 8.7% lower than the predicted value. When plotted together (figure 6.8) the EST model predicts a linear material response, while the testing results initially match the linear response, then demonstrate a stiffening before failure. This stiffening results in a lower failure displacement value that is not captured in the model. This stiffening trend was expected for the hard laminate as previously completed testing of this lamina stacking sequence demonstrated a stiffening trend.

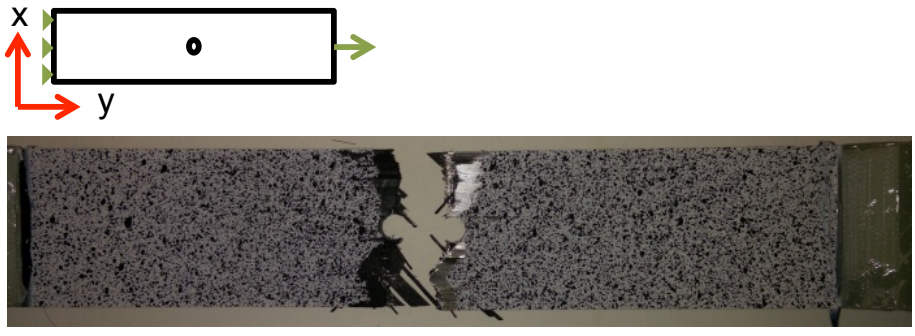

Figure 6.6: Failure mode observed in testing of hard laminate

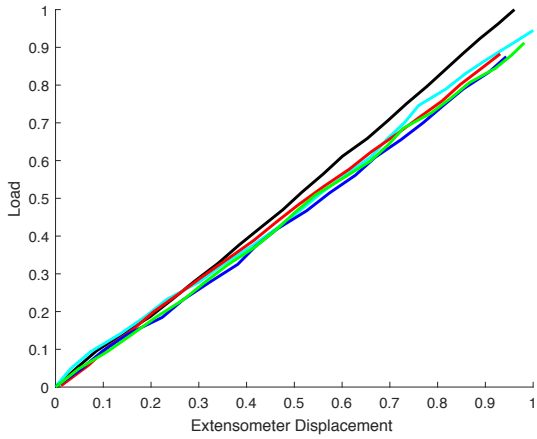

Figure 6.7: Comparison of Intermediate rate OHT Test Results on Hard laminate

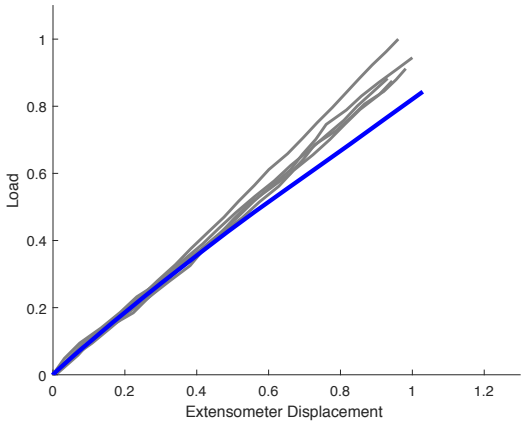

Figure 6.8: Predictive EST model compared to Test results

Test Number	Failure Load (%)	Failure Displacement(%)	Strain Rate (/s)
Average	92.3	100.4	0.17
Standard deviation	4.2	1.9	0.05
EST model	84.2	108.7	0.2
Percent difference	9	10	

Table 6.7: Hard Laminate Failure Values

Testing of the quasi laminate specimens was successfully completed for three of the five specimens. The first was preformed at a low strain rate and was successful, when the strain rate was increased to the full test speed tests two and three experienced slipping in the grips and did no reach full failure. The griping pressure of the load frame was increased and the gripping areas of the specimens were prepared with a rough sand paper instead of the emory cloth. With the changes in place the final two tests were successfully completed. Across all five tests a consistent stiffness was observed, with the two failed tests reaching 44% and 68% of the average failure load of the three successful tests. The average failure displacement

was found to be 50% and 75% lower in tests two and three respectively. When plotted together with the EST prediction it is seen that the testing and prediction are in very good agreement with the predicted failure load 9% lower than the experimental value and the failure displacement 3% lower than the measured values. The quasi laminate predictions were most accurate of the three tested layups due to their linear behavior and consistent failure mechanisms. The soft laminate predictions showed a larger sensitivity to rate than both the quasi and hard laminates, this sensitivity produced interesting test results.

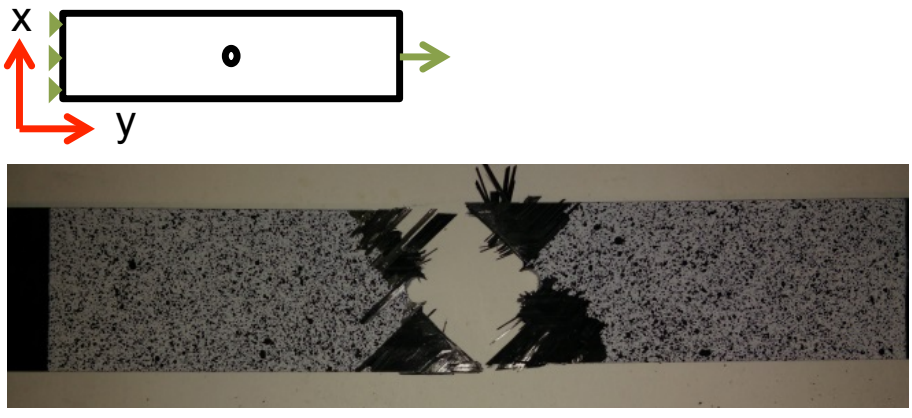

Figure 6.9: Failure mode observed in testing of Quasi laminate

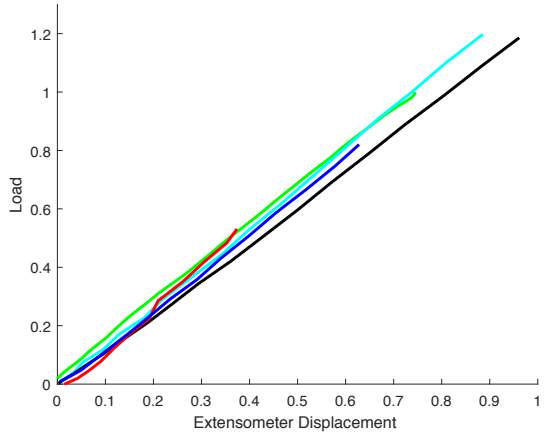

Figure 6.10: Comparison of Intermediate rate OHT Test Results on Quasi laminate

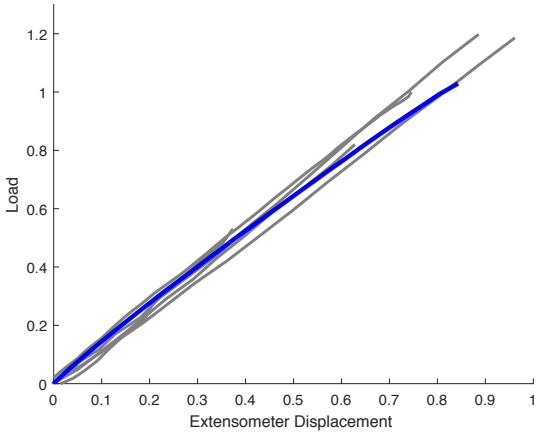

Figure 6.11: Predictive EST model compared to Test results

Test Number	Failure Load (%)	Failure Displacement(%)	Strain Rate (/s)
Average	94.1	74.7	0.15
Standard deviation	4.2	1.9	0.05
EST model	85.9	87.1	0.2
Percent difference	9	3	

Table 6.8: Quasi Laminate Failure Values

The changes implemented in the testing of the quasi laminate were also implemented on the five specimens of the soft lay up. All five soft tests were successfully completed and showed good agreement. The average failure load deviation was only 4.5% while a larger variance of 6.8% was observed in the failure displacements. The EST model predicted a failure load 15% lower and a failure displacement 29% lower than the measured values.

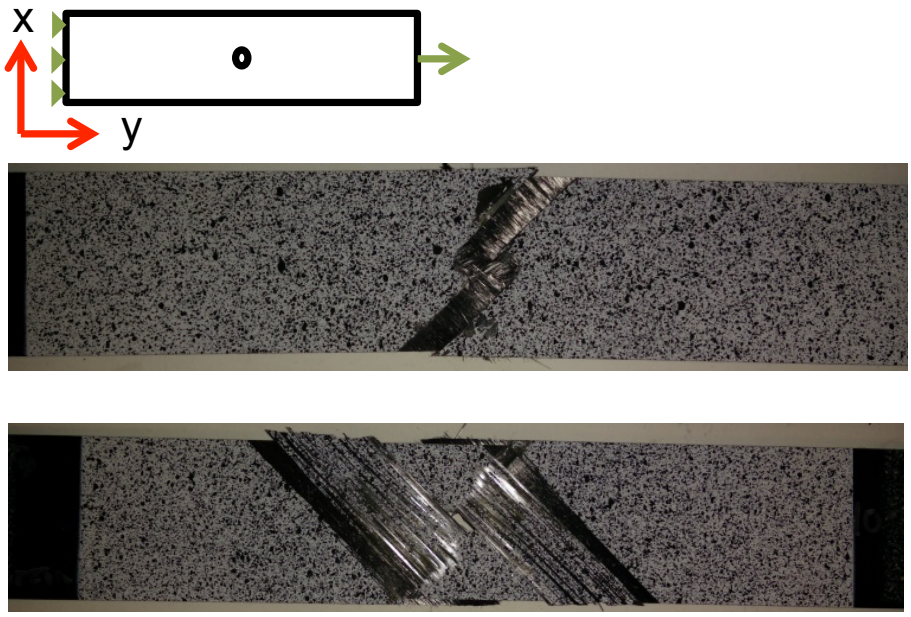

Figure 6.12: Failure modes observed in testing of Soft laminate

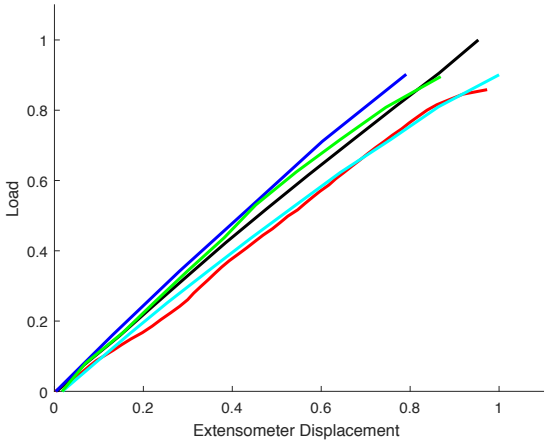

Figure 6.13: Comparison of Intermediate rate OHT Test Results on Soft laminate

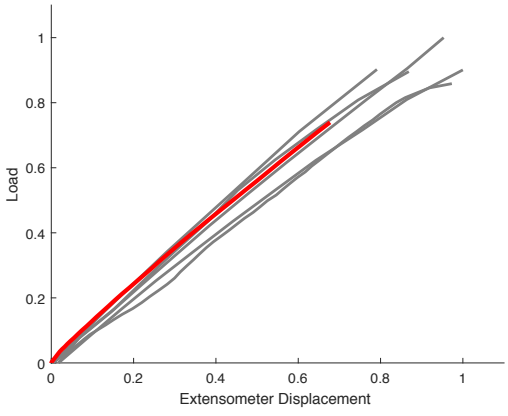

Figure 6.14: Predictive EST model compared to Test results

Test Number	Failure Load (%)	Failure Displacement(%)	Strain Rate (/s)
Average	90.8	95	0.19
Standard deviation	4.5	6.8	0.09
EST model	75	70.9	0.2
Percent difference	15	29	

Table 6.9: Soft Laminate Failure Values

6.5 Modeling Corrections

The validation testing showed that the behavior of the respective laminates (hard, quasi and soft) was accurately captured by using EST. In an effort to minimized the differences between the predictive models and the average measured values for each laminate the EST input parameters were examined for accuracy. The version of EST used for the OHT models required 18 parameters to be measured through testing and input to the model (6.5). Thirteen of these parameters are measured directly form test data (rows 1-4,9,and 11-18). The remaining five parameters (rows 5-8, and 10)are calculated from the test data and as a result subject to error. These parameters were reviewed for correctness of calculations and assumptions made.

	Input Parameter	Description
1	E_{11}	Fiber-direction stiffness
2	E_{22}	Transverse stiffness
3	ν_{12}	Poisson's ratio
4	G_{12}	Shear Modulus
5	ϕ_{11}	Initial fiber misalignment (degree)
6	es_0.....es$_{npoly}$	Transverse damage coefficients in tension
7	gs_0.....gs_{npoly}	Shear damage coefficients
8	es_{c0}....es_{npoly}	Transverse damage coefficient in compression
9	X_t	Maximum allowable axial strain in tension
10	X_c	Maximum allowable axial strain in compression
11	Y_t	Transverse lamina failure strain in tension
12	Y_c	Transverse lamina failure strain in compression
13	Z	Shear failure strain
14	G_{IT}^f	Mode I critical fracture energy of fiber under tension
15	G_{IC}^f	Mode I critical fracture energy of fiber under compression
16	G_{IT}^m	Mode I critical fracture energy of matrix under tension
17	G_{IC}^m	Mode I critical fracture energy of matrix under compression
18	G_{II}^m	Mode II critical fracture energy of matrix

Table 6.10: Test Parameters for EST input

The initial fiber misalignment (parameter 5) and maximum allowable strain in compression (parameter 10) are calculated using established methods as previously discussed. The remaining three parameters are the shear and transverse damage coefficients. These coefficients are found by fitting a polynomial curve to the G_{12}/G_{120}v.S_r curves calculated from test data (ch 4). While calculating the points on the S_r curve every data point on the stress v. strain curve was used to calculate the stiffness (i.e. G_{12}) and micro-damage (S). At the initiation of each test the measured loads are much larger than the applied

displacement, resulting in an artificially large secant stiffness. As the test progresses these values equilibrate to produce the overall linear stiffness of the material before micro-damage causes nonlinearity to occur. Previous work has used all the calculated secant stiffness values to formulate the micro-damage functions, and as a result the functions have shown a large stiffness degradation (**??**). This large degradation leads to an early trigger of failure in the EST models.

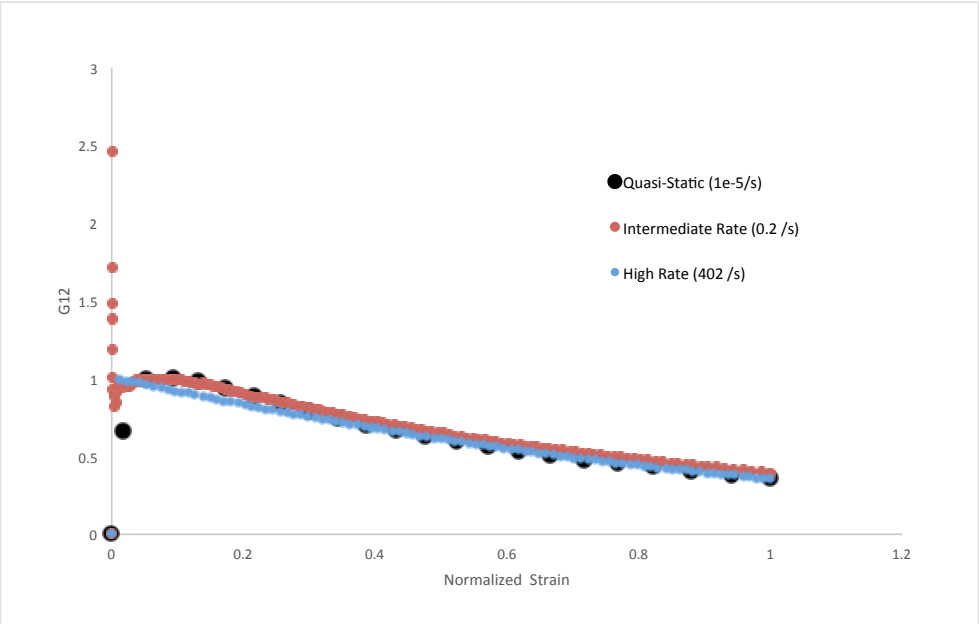

Figure 6.15: Variance of Secant stiffness (G_{12}) on a ± 45 test

The OHT prediction models were executed using the traditional analysis of stress v. strain data to produce a micro-damage function. The OHT models also predicted failure at both a lower stress and a lower strain value than was observed in the experiments. To correct this error the micro-damage function was recalculated form the point where the secant stiffness value stabilized (**??**). The new micro-damage functions showed minimal difference between rate, indicating that while the stiffness of the material is rate dependent the formation of micro-damage is not.

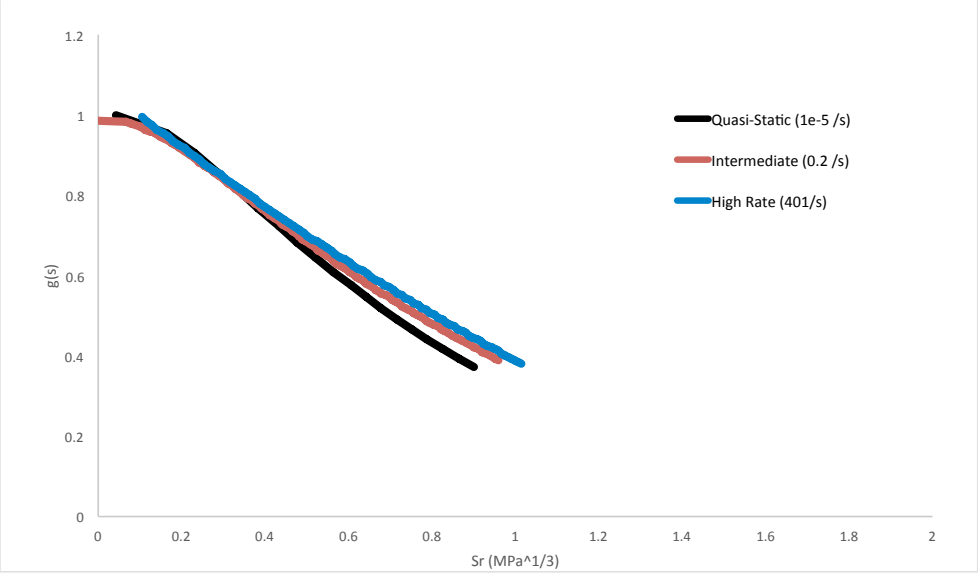

Figure 6.16: Shear micro-damage function G_{12}/G_{120}

The OHT model input parameters were updated with the newly processed data and re-run. The updated models all showed both larger failure loads and failure displacements, however the accuracy of the models varied across the laminates.

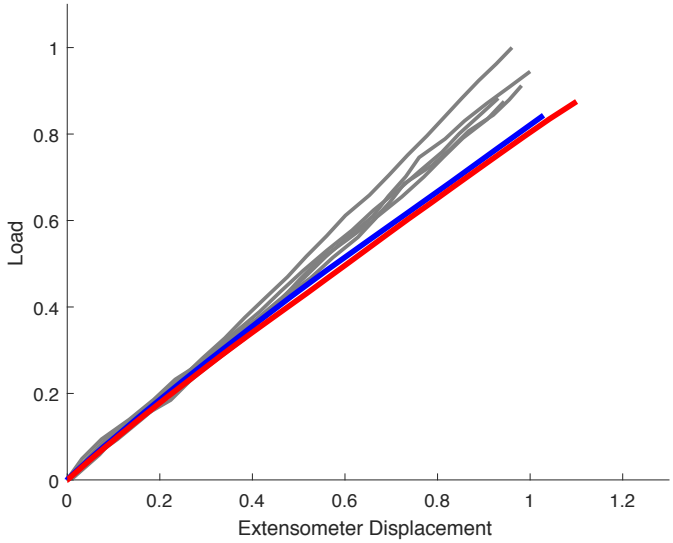

Figure 6.17: Updated EST simulation of hard laminate compared against Prediction and test results

The updated hard laminate model showed an increase in failure load and failure displacement(6.5). Both the updated model and the original model match the initial stiffness demonstrated by the tests, and fail to capture the stiffening observed in the second half of loading. The increased failure load improved the accuracy of model by 4%, while the increase in failure displacement resulted in a decrease in accuracy of the model form 10% to 15%.

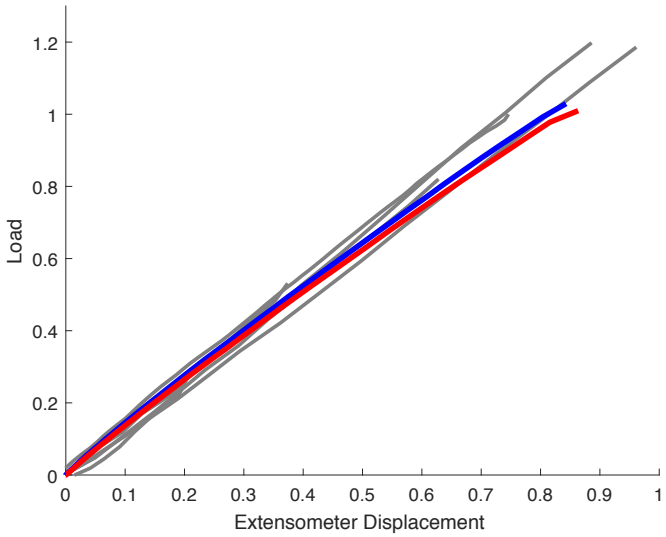

Figure 6.18: Updated EST simulation of quasi laminate compared against Prediction and test results

The updated quasi laminate model showed a softening right before failure at the end of the test. Due to the softening the failure displacement increased, capturing the average test failure value directly, while the failure load decreased. The changes resulted in a 9% increase in displacement accuracy and a 0.7% decrease in load accuracy with respect to the prediction model.

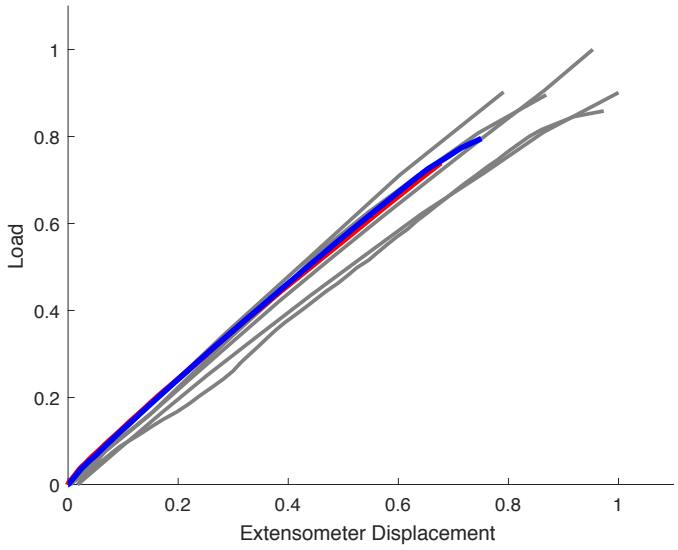

Figure 6.19: Updated EST simulation of soft laminate compared against Prediction and test results

The soft laminate model showed the largest improvement with the implemented input parameter changes. The updated model showed both a larger failure load and displacement to failure while capturing the stiffness trend demonstrated by the testing results. The model does show a slight softening toward the end of the test that is not observed in the testing, however the failure values were increased by 5.3% and 10% respectively.

Chapter 7

CONCLUSION AND DISCUSSION

This thesis established a basic characterization of a carbon fiber composite laminate material system across multiple decades of applied strain rates. This was achieved though testing of multiple layups to gather failure stress, failure strain, and stiffness values at quasi-static, intermediate and high strain rates both in tension and compression. Quasi-static and Intermediate rate tensile testing was completed on a Instron hydraulic load frame at $1e-5/s$ and $0.2/s$ strain rates. While compressive testing was completed on a MTS hydraulic load frame. The high rate compression testing was completed on a previously constructed SHPB that was calibrated for the testing purposes of this thesis. High rate tensile testing was performed on a SHTB that was designed, constructed and calibrated for the work presented in this thesis. The design of this SHTB brought to light some of the faults in Hopkinson Bar designs and testing analysis that have been presented in literature, and improved upon those errors to produce a system capable of producing repeatable and justifiable results.

The high rate tensile testing also produce novel results using a new generation of high speed camera. The camera was able to capture more frames through the duration of a test than has been previously reported, as well as recording those images at a much higher resolution. The higher resolution allowed DIC analysis to capture strain localization throughout the gage section of the specimens, indicative of micro-cracking. The formation of these micro-cracks was then correlated to the softening response of the material shown in the high rate stress-strain curves. This softening allows for the application of Schapery theory at high strain rates, as well as validating the data post processing method that was discussed earlier.

Using the measured intermediate strain rate properties as input parameters three EST OHT tension predictive models were created using Abaqus. The results of this model indicated that failure occurred earlier within the specimen as the applied rate increased

as was expected after completing rate characterization. The modeling results were then validated with OHT coupon testing of the three laminates. Coupon testing agreed well with the predictive models, further emphasizing the necessity to create models with input parameters that accurately represent the case that is being modeled.

Throughout the work presented in this thesis many testing methods have been learned, utilized, and improved upon. While the material system was rudimentarily characterized more testing is necessary to fully describe the system. The remaining tests require much further investigation, both into how to conduct them accurately at elevated strain rates and the effect of those loading rates.

7.1 Future Work

Testing of composite structures at elevate rates is a constantly developing field due to its complexity. As the loading rate increases the sensitivity of the test drastically increases, leading to a higher level of noise and potential inconsistencies in the test data. Due to this sensitivity only a few high rate testing methods are used, all with their own strengths and weaknesses. SHTB testing was used to show consistent results for a small scope of laminates in this thesis in order to measure a materials main failure characteristics. The bar design did however fall short of fully characterizing material properties such as Single Edge Notch fracture Testing, and transverse stiffness properties ($E_2 2$). These tests provided challenges for high rate testing at both ends of the spectrum. The SENT testing provided a $[90_2/0_2]_s$ laminate that was very stiff and difficult to fail within the gage section due to the large displacement allowed by the notch and the high stress required to fail the specimen at rate. The transverse stiffness is very soft and fails to early to transmit a pulse on the SHTB. Future testing of these materials would require a specific testing setup (possibly a drop tower fixture rather than a Hopkinson bar) for each case that allows a load to be easily transmitted through the specimen without undesired failures. Successfully designing a testing fixture for these extreme cases could show very interesting results and open the door for multiple other tests.

Another solution to the issues of testing specimens at rate is to alter the environment the specimens are tested in, allowing a quasi-static test to demonstrate the same characteristics

as a high rate test. It has been shown in this thesis that as the applied strain rate increases the material demonstrates a stiffening behavior. This is due to the materials inability to 'shift' and distribute load within itself, this same behavior is observed at low temperatures. If a master curve could be constructed and validated for a material system, rate testing could be conducted at variable temperatures according to the desired equivalent 'strain-rate'. The major benefit of this testing method would be the use of a hydraulic or screw driven load frame and the elimination of complex data processing and noise elimination that is necessary with many high strain rate tests.

BIBLIOGRAPHY

[1] Gilat, A., T. E. Schmidt, and A. L. Walker. "Full field strain measurement in compression and tensile split Hopkinson bar experiments." Experimental Mechanics 49.2 (2009): 291-302.

[2] Sicking, Dean Leo. Mechanical characterization of nonlinear laminated composites with traverse crack growth. Diss. Texas AM University, 1992.

[3] Bazant, Zdenek P., and Byung H. Oh. "Crack band theory for fracture of concrete." Matriaux et construction 16.3 (1983): 155-177.

[4] Pineda, Evan J., and Anthony M. Waas. "Numerical implementation of a multiple-ISV thermodynamically-based work potential theory for modeling progressive damage and failure in fiber-reinforced laminates." International journal of fracture 182.1 (2013): 93-122.

[5] Pineda, Evan Jorge. A novel multiscale physics-based progressive damage and failure modeling tool for advanced composite structures. Diss. NASA Glenn Research Center, 2012.